Small-Angle Neutron Scattering Studies of Dynamics and Hierarchical Pattern Formation in Binary Mixtures of Polymers and Small Molecules

TAKEJI HASHIMOTO

Department of Polymer Chemistry, Gradate School of Engineering, Kyoto University, Katsura, and Hashimoto Polymer Phasing Project, Exploratory Research for Advanced Technology (ERATO), Japan Science and Technology Corporation (JST), Nishikyo-ku, Kyoto 615-8510, Japan

Received 9 January 2004; revised 19 February 2004; accepted 20 February 2004
DOI: 10.1002/polb.20186
Published online in Wiley InterScience (www.interscience.wiley.com).

ABSTRACT: We present the dynamics of the composition fluctuations and pattern formation of two-component systems in both single-phase and two-phase states as studied by time-resolved small-angle neutron scattering and light scattering. Two-component systems to be covered here include not only dynamically symmetric systems, in which each component has nearly identical self-diffusion coefficients, but also dynamically asymmetric systems, in which each component has different self-diffusion coefficients. We compare the dynamic behaviors of the two systems and illuminate their important differences. The scattering studies presented for dynamically asymmetric systems highlight that stress–diffusion coupling and viscoelastic effects strongly affect the dynamics and pattern formation. For dynamically symmetric systems, we examine the universality existing in both polymer systems and small-molecule systems as well as new features concerning the time evolution of hierarchical structures during phase separation via spinodal decomposition over a wide range of wave numbers (up to four orders of magnitude). For both systems, we emphasize that polymers provide good model systems for studying the dynamics and pattern formation. © 2004 Wiley Periodicals, Inc. J Polym Sci Part B: Polym Phys 42: 3027–3062, 2004

Keywords: binary mixtures; blends; light scattering; pattern formation; phase separation; self-organization; small-angle neutron scattering; spinodal decomposition; stress–diffusion coupling

INTRODUCTION

We present here scattering studies of the time evolution of phase-separating structures via spinodal decomposition (SD) and the dynamics of composition fluctuations in single-phase mixtures for binary molecular mixtures as one of the important research topics concerning the space–time organization of molecules or supramolecules in soft matter (or complex liquids). Time-resolved small-angle neutron scattering (SANS), combined with time-resolved light scattering (LS), is used to explore the time evolution of hierarchical structures over a wide wave-number (q) scale ranging from approximately 10^{-3} to approximately 10^{0} nm^{-1} (corresponding to a length scale of approximately micrometers to nanometers). Thus, this article concerns a nonequilibrium self-assembling process of molecular systems, which involves nonlinear time-evolution equations.

What kind of hierarchical structures are of concern here? Figure 1 schematically presents a typ-

Correspondence to: T. Hashimoto (E-mail: hashimoto@alloy.polym.kyoto-u.ac.jp)

Journal of Polymer Science: Part B: Polymer Physics, Vol. 42, 3027–3062 (2004)

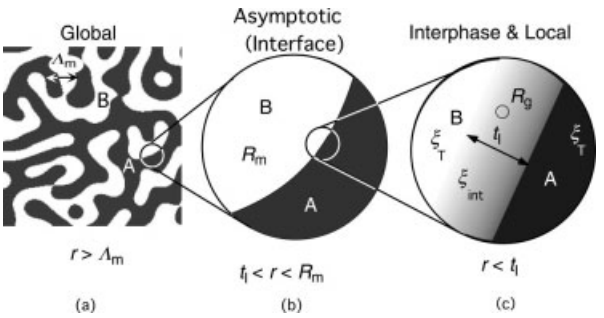

Figure 1. Schematic representation of the hierarchical structures developed from binary mixtures of A and B molecules in a phase-separation process of the late stage of SD: (a) global, (b) asymptotic (or interface), and (c) interphase and local scales. The two components have dynamic symmetry, as described in the text, and equal volume fractions.

ical real-space structure developed at a particular time in a late stage of the SD process for a binary mixture consisting of molecules A and B with nearly equal molecular sizes and with compositions of nearly equal volume fractions. The structure has been elucidated by a series of works to be presented in this article. The mixture has a two-phase structure of domains rich in A (dark region) and rich in B (bright region), which are cocontinuous in three-dimensional (3D) space and periodic with a characteristic length Λ_m [Fig. 1(a)]. A global structure (global) can be observed at $r > \Lambda_m$, r being the length scale of observation. If we focus on the structure by reducing r, so that t_I is less than R_m, we can see the interface with a mean radius of curvature R_m and an interfacial area per unit of volume (interfacial area density) Σ, t_I being a characteristic interfacial thickness [Fig. 1(c)]. In this scale, both the A-rich phase (phase 1) and the B-rich phase (phase 2) appear to have a uniform composition of A and B, which is equal to the equilibrium composition of ϕ^e_{A1} and ϕ^e_{B1} or that of ϕ^e_{A2} and ϕ^e_{B2}, predicted by the coexistence curve of the mixture and phase-separation temperature in a phase diagram (shown later in Fig. 4), in which K and J in ϕ^e_{KJ} designate the Kth component (K = A or B) in the Jth phase (J = 1 or 2) and superscript e designates equilibrium. If we further zoom in the structure so that r is less than t_I, we see the interfacial region of finite thickness t_I (Interphase), in which the average local composition of the A molecule changes between ϕ^e_{A1} and ϕ^e_{A2}, and the local composition of the A molecule located at r in the A-rich phase, $\phi_{A1}(\mathbf{r})$, and in the B-rich phase, $\phi_{A2}(\mathbf{r})$, thermally fluctuate around ϕ^e_{A1} and ϕ^e_{A2}, respectively, with thermal correlation length ξ_T (Local), as shown in Figure 1(c). In the weak segregation limit, as discussed later, t_I can be larger than the molecular size [radius of gyration (R_g) of polymers A and B], even for polymer systems, as is usually the case in small-molecule systems.

The scattering studies reveal the space–time organization of these hierarchical structures in Fourier (reciprocal) space, as illuminated in Figure 6 later, and that of various characteristic lengths, such as Λ_m, R_m, Σ^{-1}, t_I, ξ_T, and R_g. In this article, we present both polymer mixtures and small-molecule mixtures. Before going into detailed discussions, we summarize the universal features of the two systems and the unique features or merits of polymer systems with respect to nonequilibrium dynamics and pattern formation.

MERITS OF POLYMER SYSTEMS FOR STUDYING DYNAMICS AND PATTERN FORMATION

For simplicity, we consider molecules A and B to be equal in size and equal in self-diffusivity (D_c), having static and dynamic symmetry, respectively. The molecules themselves have their own temperature-dependent characteristic length (ξ_0) and characteristic time (t_0). The space-time scale of binary mixtures (ξ_c) and t_c, which characterize the characteristic length and time of thermal composition fluctuations, is related to that of molecules in terms of the following scaling laws, as is well known in the field of critical phenomena:[1]

$$\xi_c = \xi_0 \varepsilon_T^{-\nu} \tag{1}$$

$$t_c = t_0 \varepsilon_T^{-\gamma} \tag{2}$$

where

$$\varepsilon_T \equiv |\chi - \chi_c|/\chi_c$$

$$\varepsilon_T \sim \Delta T \quad \text{for } T \text{ close to } T_c, \ \varepsilon_T \sim 1 \quad \text{for } \Delta T \gg 0 \tag{3}$$

and

$$\Delta T \equiv |T - T_c| \tag{4}$$

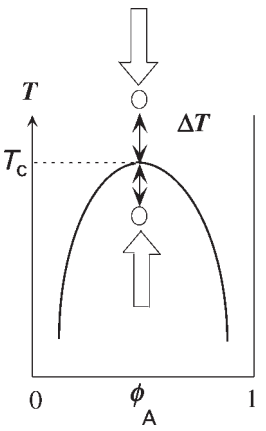

Figure 2. Schematic phase diagram of symmetric A/B mixtures and the definition of ΔT and T_c. The spatiotemporal scale of the mixtures expands as T changes along the direction of the arrows pointing toward T_c.

ν and γ are critical exponents, equal to 1/2 and 2, respectively, for the mean-field approximation. χ is a thermodynamic interaction parameter between A and B small molecules or monomeric units of polymers,[2] and χ_c is the χ parameter at a critical temperature (T_c). As our mixtures approach T_c either in a single-phase region or a two-phase region in the phase diagram, t_c and ξ_c become very large; the former and the latter are called *critical slowing down* and *critical divergence*, respectively (see Fig. 2). Thus, the space-time scale of mixtures expands as ΔT approaches 0. Because of this unique feature in critical phenomena, even for simple liquids, for which we usually observe that small structures change very rapidly, we anticipate that large structures change very slowly near the critical point. This fact has been facilitating experimental studies of critical phenomena for simple-liquid mixtures.

A basic difference between polymer mixtures and simple-liquid mixtures arises from the difference in the space-time scale of the molecules themselves, ξ_0 and t_0. It can be estimated on the basis of Gaussian statistics[2] and reptation dynamics[3,4] for polymer systems, with each component having a degree of polymerization (DP) N and a segment length a:

$$\xi_0 = N^{1/2}a \tag{5}$$

$$t_0 = \tau_1(N^3/N_e),\ \tau_1 \equiv a^2/D_1 \tag{6}$$

where polymer systems are assumed to be entangled, N being larger than N_e, the average DP between the nearest entanglement points along given chains. Here the quantities a and τ_1 correspond to the space-time scale of small-molecule systems, whereas D_1 is the self-diffusion constant of segments or small molecules. When N is 10^4 and N_e is 10^2, as may be found for typical polymer systems,

$$\xi_0 = 10^2 a,\ t_0 = 10^{10}\tau_1 \tag{7}$$

Thus, the space-time scale of typical polymer systems is extremely large in comparison with that of small-molecule systems, and this gives such an important result that in polymer systems larger structures evolve very slowly at a given ΔT, in comparison with those of small-molecule systems. This result facilitates quantitative and precise experimental investigations of nonequilibrium dynamics and processes for polymer systems.[5]

If we set our experimental conditions for polymer systems such that the space-time scale of our observation is much larger than that of the polymer molecules themselves, we anticipate that the dynamics and processes of polymer mixtures will be universal with those of small-molecule mixtures, except for the extraordinary expansion of the space-time scale in polymers. If we set the space-time scale of observation to be comparable to or less than that of the polymer molecules, we anticipate unique features of polymers that cannot be expected for small molecules. A good example is a q dependence of the Onsager kinetic coefficient at $r \lesssim R_g$ or $q \gtrsim 1/R_g$, as elaborated by deGennes,[6] Pincus,[7] Binder,[8] and Akcasu.[9]

DYNAMIC ASYMMETRY AND STRESS–DIFFUSION COUPLING: THEORETICAL BACKGROUND

In this article we deal with both dynamically symmetric and asymmetric mixtures. The former mixtures were briefly discussed in the previous section. Most small-molecule mixtures have dynamic symmetry, and so the nonequilibrium dynamics and processes for this family have been relatively well explored in comparison with those of the other family with dynamic asymmetry. In the former case, we can discuss universality in the phase-separation behavior of polymer mixtures and small-molecule mixtures.[10,11] The polymer mixtures can be good model systems that

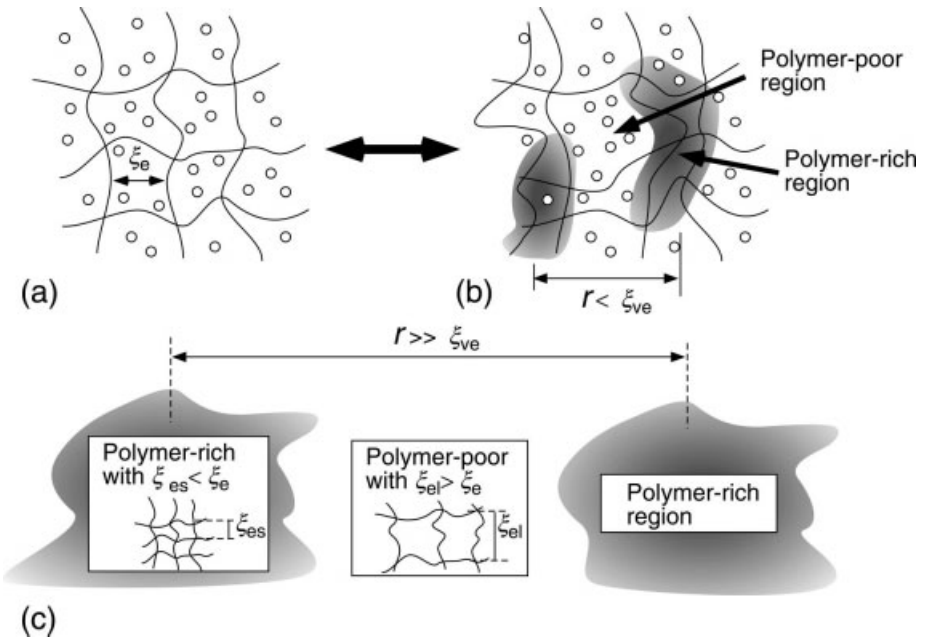

Figure 3. Schematic representation of stress–diffusion coupling and viscoelastic effects in polymer solutions. The lines and circles in parts a and b represent polymer chains and solvents, respectively. Part a represents semidilute solutions with relatively homogeneous polymer concentrations at $r > \xi_e$, whereas parts b and c represent those with concentration fluctuations at a short length scale and at a larger length scale, respectively. In parts b and c, the shaded regions designate polymer-rich regions ($\xi_{es} < \xi_e$), whereas the unshaded regions designate polymer-poor regions ($\xi_{el} > \xi_e$). Parts b and c differ in r for the concentration fluctuations. In part c, the solvents are not shown. Based on ref. 18.

enable us to pursue experimental studies of the nonequilibrium dynamics and processes to a level that cannot be easily attained with small-molecule mixtures.[5]

In dynamically asymmetric mixtures, the component molecules have different mobility (self-diffusivity) values, as for mixtures of polymers with different molecular weights or dispersions of colloidal particles in a solvent, although colloids themselves are not molecules but can be considered supramolecules. In this case, phase-separation dynamics and processes involve a new problem, stress–diffusion coupling,[12–14] which is not encountered in dynamically symmetric mixtures. Because of this effect, the phase-separation dynamics and processes,[15–18] as well as the dynamics of composition fluctuations, in single-phase systems[19] are affected by viscoelastic relaxation and involve a new characteristic length scale of the so-called viscoelastic length (ξ_{ve}), as elaborated by Doi and Onuki.[12,13]

A good example showing this effect is a semidilute polymer solution, that is, a binary mixture of a high-molecular-weight polymer and a solvent, as depicted in Figure 3.[18] Suppose that concentration fluctuations of a characteristic length r are developed, as shown in Figure 3(b,c), from an entangled polymer solution with a statistically homogeneous polymer concentration with an average mesh size (ξ_e) between the entanglement couplings [Fig. 3(a)]. In Figure 3(b,c), the shaded and unshaded areas represent regions with higher and lower polymer concentrations with smaller and larger mesh sizes (ξ_{es} and ξ_{el}, respectively). If the growth rate of thermally activated concentration fluctuations (Γ_r) is faster than the relaxation rate of the entangled polymer networks (Γ_e), the concentration fluctuations will build up local stress. Furthermore, the built-up stress and its spatial variation will be relaxed at rate Γ_e, which is characterized by the viscoelastic properties of the system. The local variation of the stress field in the solution affects the free-energy functional mathematical terminology of the system and hence the diffusion processes of the system.

Thus, stress–diffusion coupling occurs when Γ_r is greater than Γ_e, and the coupling suppresses the dynamics of concentration fluctuations. If length r is comparable to ξ_e [Fig. 1(b)], this criterion for the stress–diffusion coupling should be fulfilled. However, for large length-scale concentration fluctuations with $r \gg \xi_e$, as shown in Figure 3(c), Γ_r is extremely small, and such fluctuations will be developed under a situation in which the built-up stress is completely relaxed as a result of large-scale rearrangements of entanglement couplings via disentanglement processes; this results in the formation of entangled regions with ξ_{es} in polymer-rich regions and ξ_{el} in polymer-poor regions [Fig. 3(c)]. Hence, this case would not involve such stress–diffusion coupling.

We can envision a screening length (ξ_{ve}) for the stress–diffusion coupling: if r is greater than ξ_{ve}, the coupling is screened out, but if r is less than ξ_{ve}, the coupling is important and is expected to become increasingly important with decreasing r because Γ_r is approximately r^{-2} and local stress buildup and its inhomogeneity increase with decreasing r. Thus, the coupling would affect the transport property of the system, the Onsager kinetic coefficient [$\Lambda(q)$]. At large q values (satisfying $q\xi_{ve} > 1$), this causes a suppression of $\Lambda(q)$ according to $\Lambda(q) \sim q^{-2}$, as discussed later. $q(\sim r^{-1})$ is the wave number of a Fourier mode of the concentration fluctuations, whose intensity [$I(q)$] is detected by scattering experiments at a particular magnitude of the scattering vector ($\mathbf{q}$):

$$q = (4\pi/\lambda)\sin(\theta/2) \tag{8}$$

where λ and θ are the wavelength of the incident beam and the scattering angle in the solutions, respectively.

It is striking, though quite natural, to recognize that phase separation couples with viscoelastic relaxation and hence the viscoelastic properties of the system. The research along this line is fascinating, as it involves various fundamental problems in physical science, such as (1) the nonequilibrium statistical mechanics of phase transitions and structure formation in thermodynamically unstable and metastable systems, (2) rheology, (3) scattering and structural characterization, and (4) the polymer physics of asymmetric mixtures and semidilute polymer solutions.

Doi and Onuki[12–14] formulated a time-evolution equation for composition fluctuations for dynamically asymmetric systems:

$$\frac{\partial}{\partial t}\,\delta\phi(\mathbf{r}, t) = -\Lambda\nabla\cdot\left[\nabla\frac{\delta F}{\delta\phi} - \alpha_a\nabla\cdot\ddot{\sigma}(\mathbf{r}, t)\right] + \zeta(\mathbf{r}, t) + (\text{hydrodynamic term}) \tag{9}$$

where $\delta\phi(\mathbf{r},t) \equiv \phi(\mathbf{r},t) - \phi_0$ represents fluctuations of local composition $\phi(\mathbf{r},t)$ of a component (e.g., A) in mixtures at a local position $\mathbf{r}$ and time t from its average value ϕ_0. $F = F\{\delta\phi\}$ is the free-energy functional of $\delta\phi(\mathbf{r},t)$, and $\delta F/\delta\phi$ is the variational derivative of F with respect to $\delta\phi(\mathbf{r},t)$. α_a is the so-called dynamic asymmetry parameter defined by

$$\alpha_a = |D_A N_A - D_B N_B|/(D_A N_A \phi_B + D_B N_B \phi_A) \tag{10}$$

where D_K, N_K, and ϕ_K are the self-diffusivity, DP, and volume fraction of the Kth component in mixtures (K = A or B). In eq 10, α_a is equal to ϕ_A^{-1} for polymer solutions, ϕ_A being the volume fraction of the polymer. $\ddot{\sigma}(\mathbf{r},t)$ is the local stress tensor, and $\zeta(\mathbf{r},t)$ is the random thermal force expressed by the following fluctuation–dissipation theorem:

$$\langle\zeta(\mathbf{r}, t)\zeta(\mathbf{r}', t')\rangle = -2k_B T\Lambda\nabla^2\delta(\mathbf{r} - \mathbf{r}')\delta(t - t') \tag{11}$$

where k_B and T are the Boltzmann constant and absolute temperature, respectively, and $\langle x\rangle$ denotes thermal average of quantity x. Cahn, Hilliard, and Cook[20–22] and Ginzburg and Landau[23] originally introduced the first and third terms on the right-hand side (rhs) of eq 9, whereas Kawasaki and Ohta[24] introduced the hydrodynamic term. Doi and Onuki[12–14] further generalized the equation by incorporating the stress term associated with the dynamic asymmetry and the stress–diffusion coupling (the second term in rhs of eq 9).

If the systems to be considered are dynamically symmetric, $D_A N_A$ is equal to $D_B N_B$, and hence α_a is equal to 0, the second term in rhs of eq 9 vanishes. Consequently the equation reduces to the well-known Cahn–Hilliard–Cook (CHC) equation or the time-dependent Ginzburg–Landau (TDGL) equation. If $\delta\phi(\mathbf{r},t)$ is small and the hydrodynamic term can be neglected, eq 9 can be linearized, and the linearized equation in q space is given by[12]

$$\frac{\partial}{\partial t}\,\delta\phi(q, t) = \Lambda(q)q^2\left[(r_0 - Cq^2)\delta\phi(q, t) - \frac{4}{3}\alpha_a^2\int_0^t dt' G(t - t')\frac{\partial}{\partial t'}\,\delta\phi(q, t')\right] + \zeta(q, t) \tag{12}$$

The first term in rhs of eq 12 is obtained on the basis of the Ginzburg–Landau (GL) expansion of the free-energy functional. $r_0 \equiv -(\partial^2 f/\partial\phi^2)_0$ (f being the free-energy density of the mixture) is a parameter related to thermodynamic driving force for composition fluctuations, being positive in a phase-separation condition, which therefore tends to increase fluctuations, and negative for mixtures in a single-phase state, which decays thermally activated fluctuations (as discussed later). C is a positive constant related to the gradient free energy due to the nonlocality of interactions.[6,22,25] $G(t)$ is the relaxation function of the shear modulus:

$$G(t) = \sum_{i=1}^{n} G_i \exp(-t/\tau_i) \tag{13}$$

where G_i and τ_i are the strength and relaxation time for the ith relaxation process. $\zeta(q,t)$ is given by

$$\langle \zeta(q, t)\zeta(q', t')\rangle = 2k_B T\Lambda(q)q^2\delta(t - t')(2\pi)^3\delta(q + q') \tag{14}$$

In eq 12, we assume that the systems to be considered are isotropic, and so **q** is replaced by q.

The second term in rhs of eq 12 represents the stress built up by the increase in the composition fluctuations, $\partial\delta\phi(q,t')\partial t'$. Because the integral is always positive, the stress term tends to suppress the growth rate of composition fluctuations or the relaxation rate in single-phase mixtures, as we naturally anticipate. Thus, interestingly enough, the dynamics are affected by the stress–relaxation process and hence by the mechanical properties of the system. When the stress relaxes more quickly than the composition fluctuations (this is usually the case near the spinodal line), this integral is simplified so that the term $\partial\delta\phi(q,t')\partial t' \cong \partial\delta\phi(q,t)\partial t$ is put outside the integral. Under this situation, we obtain

$$\frac{\partial}{\partial t}\,\delta\phi(q, t) = \frac{\Lambda(q)}{1 + \xi_{ve}^2 q^2} \times q^2(r_0 - Cq^2)\delta\phi(q, t) + \zeta(q, t) \tag{15}$$

where ξ_{ve} is defined by

$$\xi_{ve} \equiv \left[\frac{4}{3}\,\alpha_a\Lambda(0)\eta_0\right]^{1/2} \tag{16}$$

and η_0 is the zero-shear viscosity given by

$$\eta_0 \equiv \sum_{i=1}^{n} G_i\tau_i \tag{17}$$

$\Lambda(0)$ in eq 16 is expressed by

$$\Lambda(0) = \phi_A\phi_B(D_A N_A\phi_B + D_B N_B\phi_A)\,\nu_0/k_B T \tag{18}$$

where v_0 is defined by

$$\nu_0 \equiv (\phi_A/\nu_A + \phi_B/\nu_B)^{-1} \tag{19}$$

with v_K (K = A or B) being the molar volume of the Kth monomeric unit.

The viscoelastic effect gives a renormalization effect with respect to the Onsager kinetic coefficient, giving rise to an effective suppression of $\Lambda(q)$. This suppression depends on a product of ξ_{ve} and q; the larger the value is, the larger the suppression is. ξ_{ve} is a unique and important characteristic length of the system that depends on the dynamic properties, most importantly on the dynamic asymmetry parameter α_a, but it also depends on the zero-shear viscosity and the small q limit of the Onsager coefficient. We later discuss quantitatively the effects of the stress–diffusion coupling and viscoelastic length on the dynamics of the composition fluctuations and pattern formation with a time-resolved SANS technique

The effects of dynamic asymmetry disappear for $q \ll 1/\xi_{ve}$ or $r \gg \xi_{ve}$ or $t \gg \tau_{ve} \equiv \xi_{ve}^2/D$ [τ_{ve} and D are the relaxation time for the viscoelastic effects (viscoelastic time) and the mutual diffusion coefficient, respectively]. In other words, the dynamically asymmetric effects are insignificant in the hydrodynamic regime of a large space-time scale of observation.

TIME EVOLUTION OF SELF-ORGANIZED STRUCTURES VIA SD IN DYNAMICALLY SYMMETRIC SYSTEMS

Time Evolution of Hierarchical Structures in Symmetric Polymer Mixtures

Systems to be Studied

Here we investigate a binary critical mixture of amorphous polymers far above their glass-transition temperatures (T_g's) so that the mixture is liquidlike for the long time limit of concern here.

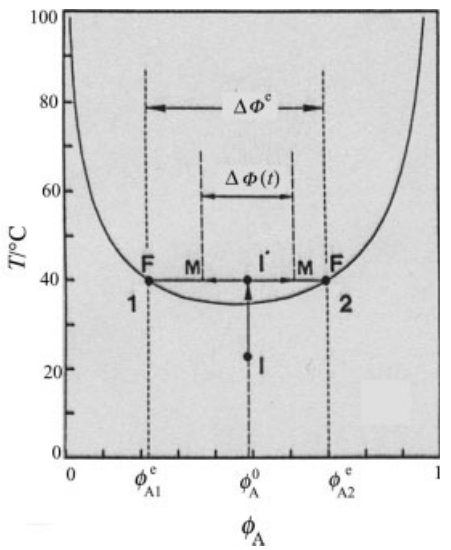

Figure 4. Coexistence curve, for a DPB/HPI mixture, calculated on the basis of the Flory–Huggins theory[2]. Component A is DPB. The data are based on ref. 26.

We study this system as a model system for dynamically symmetric systems. The mixture, composed of deuterated polybutadiene (DPB) and protonated polyisoprene (HPI), has a lower critical solution temperature (LCST) phase diagram, whose theoretical coexistence curve is shown in Figure 4.[26] We quench the mixture at an equilibrium state I in a single-phase state to state I′ inside the spinodal phase boundary. The mixture is thermodynamically unstable at I′, and so the composition fluctuations grow with time via SD,[20] generating domains rich in component A (DPB) and domains rich in component B (HPI). The composition difference [$\Delta(\Phi(t)$] of component A between the two domains increases with time and reaches an equilibrium value [$\Delta\Phi^e$] in the late stage of SD; there, the size of the domains still increases, and interfacial area keeps decreasing. The equilibrium state (F) at the phase-separation temperature (T) is composed of two macrophases, 1 and 2, with ϕ_A equal to ϕ^e_{A1} and ϕ^e_{A2}.

We are interested in studying the self-assembling process, mechanism, and dynamics involved in this phase transition with a combined time-resolved SANS and LS technique. The technique enables us to study the space–time organization of the structure over a wide length scale r from 1 nm to 10 μm (or over a wave-number scale q from 10^{-4} to 10^{0} nm^{-1}) and over a wide time scale from 1 to 10^4 min, covering the early to late stages of SD.[5] A basic time-evolution equation of the order parameter $\delta\phi(\mathbf{r},t)$ (space–time composition fluctuations of one component) in our system is given by a generalized TDGL equation for binary fluids, which takes into account hydrodynamic effects.[24] The system is nearly dynamically symmetric, with a very small value for the asymmetry parameter ($\alpha_a = 0.16$).

We investigate the pattern formation in our self-organizing system through time changes in the elastic scattering intensity of neutrons and light [$I(q,t)$], which corresponds to the intensity of the Fourier mode of the fluctuations with q at time t after the onset of SD. Experimentally, q is varied through changes in the magnitude of $\mathbf{q}$ through changes in θ and/or λ, as obviously shown in eq 8. The experimental setup and conditions of SANS and LS have been described in detail elsewhere.[26,27]

The DPB sample has a weight-average DP of $N_w = 1.7 \times 10^3$ and a heterogeneity index (characterizing the polydispersity in DP) of $N_w/N_n = 1.04$, where N_n is the number-average DP. HPI has values of $N_w = 2.0 \times 10^3$ and $N_w/N_n = 1.04$. We investigated a critical mixture of DPB and HPI with a 47/53 (v/v) composition ratio. Here we report our results at 40 °C. SANS studies in the single-phase state have allowed us to determine the following characteristics of the mixture.[26,27] First, it has a spinodal temperature (T_s) of 36.1 °C, which is well above the T_g values of −95 °C for DPB and −72 °C for HPI. Second, the mean-filed Flory interaction parameter per monomer unit (χ_{eff}) was evaluated as a function of T. Third, this result gives the parameter ϵ_T, which characterizes thermodynamic driving force for the phase separation at the experimental temperature of T = 40 °C:

$$\varepsilon_T \equiv (\chi_{eff} - \chi_s)/\chi_s = 0.0668 \qquad (20)$$

$\epsilon_T \ll 1$ indicates that our system is in a weak segregation limit. This situation is also confirmed later by a large value of t_I:

$$t_I \cong 7R_g \qquad (21)$$

where R_g is the radius of gyration of DPB and HPI. The value for each has been separately estimated to be approximately identical, 11.6 nm. Fourth, ξ_T has been estimated to be 25 nm. This value is larger than R_g, reflecting again the weak segregation limit. Fifth, ϵ_T is equal to 0.0668 $\gg 1/N$ ($\cong 5 \times 10^{-4}$), and so the system is far outside the critical region, as specified by the Ginzburg

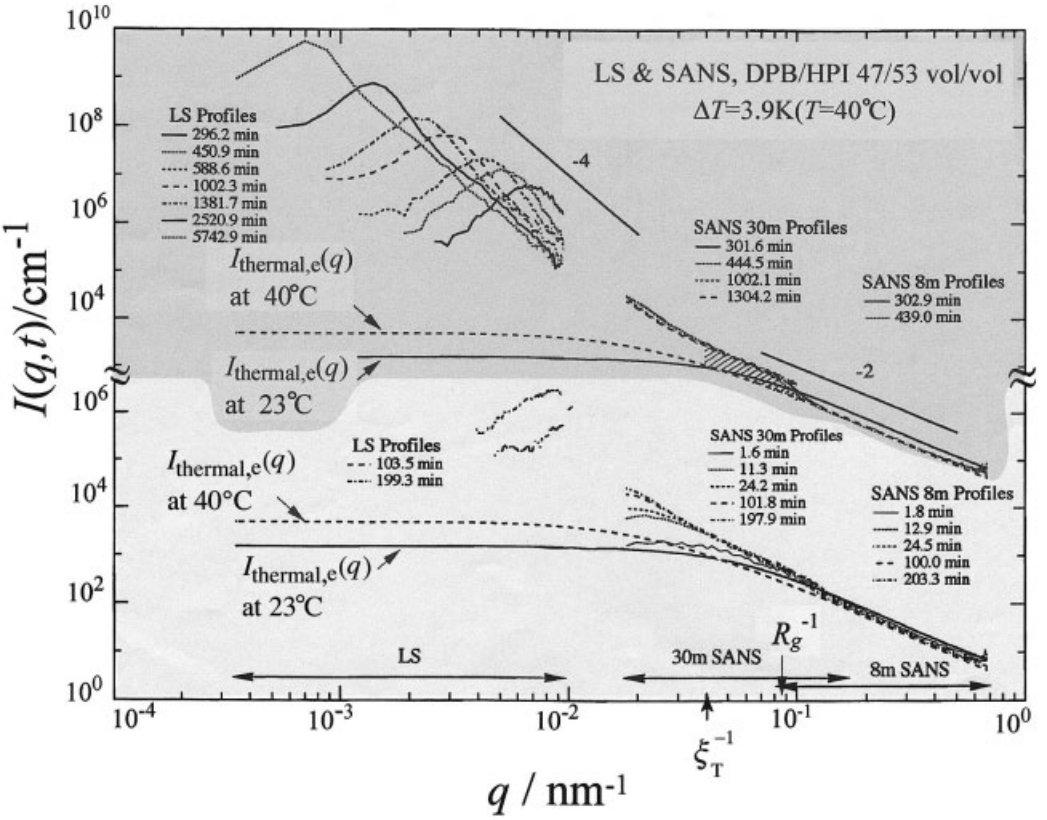

Figure 5. Time-resolved LS (3×10^{-4} nm$^{-1} < q < 10^{-2}$ nm^{-1}) and SANS profiles (2×10^{-2} nm$^{-1} < q < 7 \times 10^{-1}$ nm^{-1}) after the onset of SD at 40 °C for a DPB/HPI mixture (see Fig. 4 for its phase diagram). The upper half of the figure (shown on the dark gray background) presents the scattering profiles from 296.2 to 5742.9 min for LS profiles, from 301.6 to 1304.2 min for 30-m SANS profiles, and from 302.9 to 439.0 min for 8-m SANS profiles. These scattering curves present the absolute scattered intensity $I(q,t)$ from 10^0 and 10^{10} cm^{-1}. The lower half of the figure (shown on the bright gray background) presents the scattering profiles from 103.5 to 199.3 min for LS profiles, from 1.6 to 197.9 min for 30-m SANS profiles, and from 1.8 to 203.3 min for 8-m SANS profiles. These scattering curves present the absolute scattered intensity $I(q,t)$ from 10^0 to 10^7 cm^{-1}. The upper and lower halves of the figure indicate the profiles in the late stage of SD and the early to intermediate stages of SD, respectively. The data are based on ref. 26.

criterion.[3,8] Thus, the evolution of $\phi(r,t)$ and $I(q,t)$ should follow the mean-field behavior.

Time Evolution of Scattering over a Wide q Range

Figure 5 shows double-logarithmically the absolute scattering intensity profile $I(q,t)$ (cm^{-1}) as a function of q at various times after the onset of SD.[26,27] The absolute SANS intensity has been obtained according to a standard method. The absolute LS intensity has been obtained according to a special method that is discussed later in conjunction with Figure 6. Some of the data at $q \leq 10^{-2}$ nm^{-1} have been obtained by LS, and the data at $2 \times 10^{-2} \leq q \leq 7 \times 10^{-1}$ nm^{-1} have been obtained with both 30- and 8-m SANS instruments at NIST (National Institute of Standards and Technology). The three sets of data cover a wide q range of about four orders of magnitude. There is still a small gap in the q range (1×10^{-2} to 2×10^{-2} nm^{-1}) that cannot be covered by our method. We request that our readers look at the LS profiles and the 30-m SANS profiles across the gap as follows. The 30-m SANS profiles at 101.8 and 197.9 min should be smoothly connected to the LS profiles at 103.5 and 199.3 min, respectively; the 30-m SANS profile at 1002.1 min

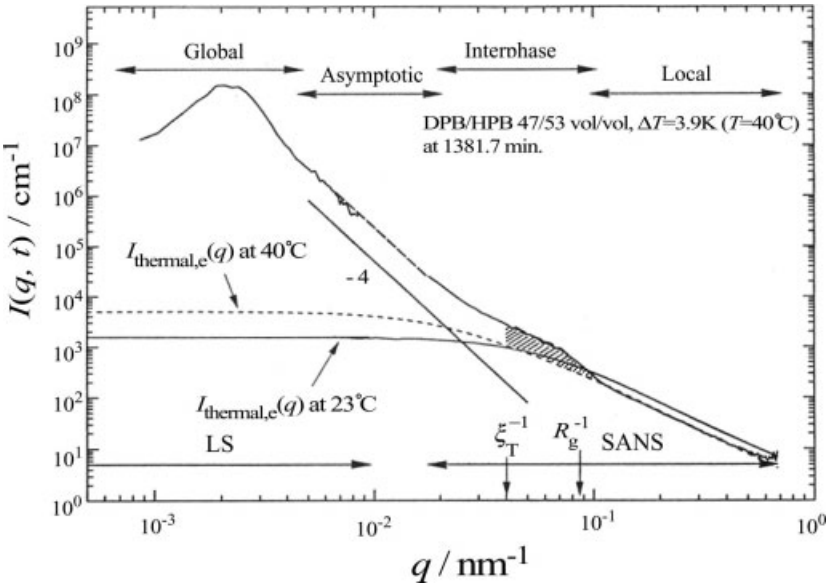

Figure 6. LS and SANS profile at $t = 1381.7$ min (corresponding to $\tau \cong 30$) in the late stage of SD, which covers various q regimes: global, asymptotic (or interface), interphase, and local. The sample was the same one used for Figures 4 and 5. The data are based on ref. 26.

should be smoothly connected to the LS profile at 1002.3 min. The arrows show the wave numbers corresponding to ξ_T^{-1} and R_g^{-1}. The lower half of the figure, including the LS profiles at 103.5 and 199.3 min, the 30-m SANS profiles from 1.6 to 197.9 min, and the 8-m SANS profiles from 1.8 to 203.3 min, presents the time change in the profiles in the early to intermediate stages of SD, whereas the upper half presents the profiles in the late stage. The LS profiles could not be detected at a time scale shorter than 103.5 min, simply because the LS intensities were weaker than the background noise level of our experiment setup. We might imagine that the LS profile at 1.6 min is close to the intensity level of $I_{\text{thermal,e}}(q)$ at 23 °C (shown by the solid line) and that those at 11.3 and 24.2 are close to the intensity level between $I_{\text{thermal,e}}(q)$ at 23 °C and that at 40 °C (broken line), as will be discussed later. The time scale covered is about four orders of magnitude after the onset of SD, and the intensity scale extends over nine orders of magnitude.

We first focus our attention on the early to intermediate stages of SD. After the onset of SD, a scattering maximum appears at the peak scattering vector, $q_m \cong 2 \times 10^{-2}$ nm^{-1}, in the q range covered by the 30-m SANS instrument. The maximum intensity increases with time without a significant change in q_m up to about 10 min, and then q_m rapidly shifts toward smaller q values, disappears in the q gap, and appears again at the higher q limit covered by LS (see the two profiles at 103.5 and 199.3 min and Fig. 7). The solid curve shows the equilibrium scattering in the single-phase state at 23 °C measured before the temperature quench, with the 30- and 8-m SANS apparatus down to the lower q limit of the 30-m instrument. The solid line below this q limit was estimated by a best fitting of the scattering function based on the RPA (random phase approximation) theory[3,28] to the experimental SANS profile.[29] The scattered intensity at $q > 1/R_g$ decreases with time after the onset of SD at 40 °C, reaching an equilibrium value in the late stage at about 250 min, as will be detailed later. This equilibrium scattering, designated $I_{\text{thermal,e}}(q)$ and shown by a broken line, corresponds to composition fluctuations from phase-separated domains with the equilibrium composition of component A equal to ϕ_{A1}^e and ϕ_{A2}^e. The intensity in the q range lower than 10^{-1} nm^{-1} $\cong R_g^{-1}$ increases, but the intensity in the q range higher than R_g^{-1} decreases with time, and this results in the least change in the intensity in q centered at R_g^{-1}. The change in the equilibrium scattering profile obviously reflects that in the equilibrium state of the mixtures.

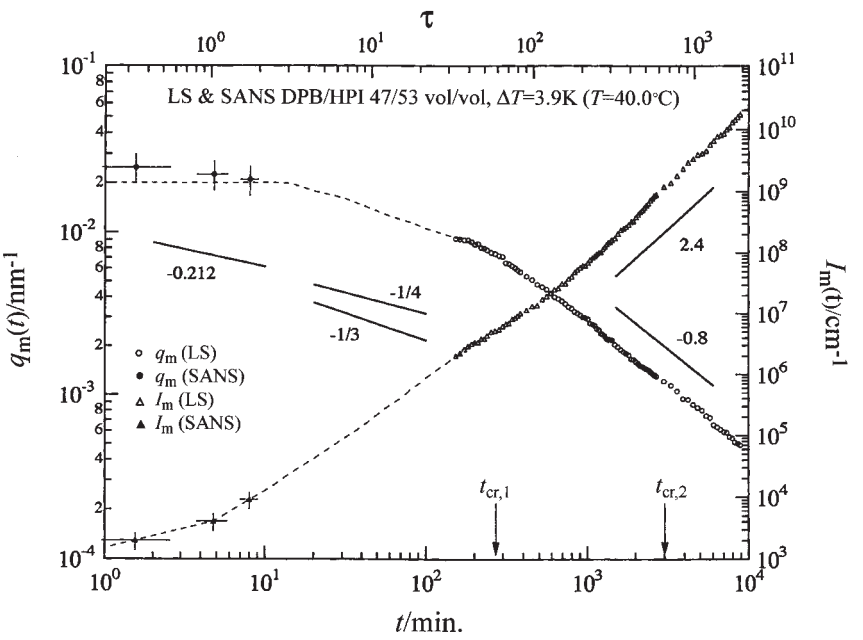

Figure 7. Time changes in $q_m(t)$ and $I_m(t)$ in a double-logarithmic scale. The sample was the same one used for Figures 4–6. The data are based on ref. 26.

Next we discuss the time change of the profile in the late stage (see the upper part of Fig. 5). The scattering at high q values, as shown by SANS, does not change much with time, as highlighted by the hatched region in the figure, almost reaching an equilibrium state. There is a very small decrease in the intensity at $q \leq {\xi_T}^{-1}$ (4×10^{-2} nm^{-1}) but no change at $q \geq {\xi_T}^{-1}$. This important feature has been elucidated for the first time in this work. Here the small decrease in the intensity reflects a decrease in the interfacial area density with time, as will be discussed later. On the contrary, the scattering at small q values, as shown by LS, still changes with time. The time-independent part of the profile in ${\xi_T}^{-1} \leq q \leq {R_g}^{-1}$ has an excess intensity (as highlighted by hatching) with respect to that from the equilibrium intensity [$I_{thermal,e}(q)$] at 40 °C (broken line). This is also a very important result, which has never been elucidated in earlier reports. We shall discuss this scattering later.

Hierarchical Structure

Figure 6 highlights the scattering profile at a particular time in the late stage (at $t \cong 1381.7$ min). The intensity in the q gap was interpolated by a broken line.[26] Because the SANS intensity profile has been calibrated into the absolute intensity according to a standard method, the interpolation can convert the relative corrected LS intensity into the absolute intensity. We propose here that the profile can be classified into four regimes: (1) a global regime ($q < 4.5 \times 10^{-3}$ nm^{-1}), (2) an asymptotic (or interface) regime ($4.5 \times 10^{-3} < q < 2 \times 10^{-2}$ nm^{-1}), (3) an interphase regime ($2 \times 10^{-2} < q < 1 \times 10^{-1}$ nm^{-1}) and (4) a local regime ($1 \times 10^{-1} < q < 7 \times 10^{-1}$ nm^{-1}). The four regimes correspond to those discussed previously in conjunction with Figure 1. As elucidated later, the q range for each regime is generally time-dependent; for example, the global regime shifts toward smaller q values with time, but the local regime is time-independent. The asymptotic and interphase regimes appear in the late stage. The former shifts toward smaller q values with time, and this appears to expand the q range for the interphase regime. We later discuss the time evolution of the structures in each regime.

The time change in the scattering function over the very wide q and t scales shown in Figures 5 and 6 reveals one important conclusion concerning the space–time organization of the structures in our system: the structure with a shorter characteristic length r or a higher wave number q relaxes toward equilibrium faster than that having a longer r or lower q (**conclusion 1**). This

conclusion seems to be reasonable and universal because Fourier modes of the structures having a higher q value have a higher gradient free energy [$(\nabla\phi)^2 \sim q^2$] and hence relax more quickly toward a new equilibrium at the phase-separation temperature. For our particular system, the structures shown by SANS (with $q \geq 2 \times 10^2$ nm^{-1}) essentially reach equilibrium in the late stage of SD.

Global Regime

Space–Time Organization of the Global Structure

Scattering function $I(q)$ for systems with Λ_m generally depends on mean-squared fluctuations of scattering power $\langle\eta^2\rangle$ and characteristic volume Λ_m^3, both of which affect the absolute scattering intensity, and shape factor $F(q)$, which affects the intensity distribution of scattering with respect to q. $\langle\eta^2\rangle$ is related to fluctuations of the refractive index for LS, the scattering length for SANS, and the electron density for small-angle X-ray scattering (SAXS), which are commonly described in terms of mean-squared composition fluctuations ($\langle\Delta\phi^2\rangle$). Therefore, the scattering function at particular time t is generally given by

$$I(q, t) = (\text{const.})\langle\Delta\phi(t)^2\rangle q_m(t)^{-3}F(x) \quad (22a)$$

On the basis of eq 22a, we can define a scaled structure factor[30,31] that characterizes the shape of the structure self-organized with time:

$$F(x) \equiv I(q, t)q_m(t)^3,\ x \equiv q/q_m(t) \quad (22b)$$

In eq 22a, we use the relationship between q_m and Λ_m ($\Lambda_m = 2\pi/q_m$).

The time evolution of the global structure can be characterized by the time changes in the wave number [$q_m(t)$] and intensity [$I_m(t)$] at the peak of the SANS or LS scattering function [$I(q,t)$] and by the time change in the shape of the scattering profile with the peak centered at $q = q_m(t)$. If the shape of the growing structure under consideration is statistically identical and only its characteristic length is changing with time t, $F(x)$ becomes independent of t (dynamic self-similarity). $q_m(t)$ is related to the characteristic length scale [$\Lambda_m(t)$] of the global structure [$q_m(t) = 2\pi/\Lambda_m(t)$], and I_m is related to $\langle\Delta\phi(t)^2\rangle$, $q_m(t)$, and $F(x = 1)$.

Figure 7 presents double-logarithmically the time changes in $q_m(t)$ and $I_m(t)$ as observed by SANS (at $t \leq 10$ min) and LS (at $t \geq 100$ min). τ indicates the reduced time, that is, the real time t renormalized by t_c of the mixture ($\tau \equiv t/t_c$). $q_m(t)$ decreases with t from about 2.5×10^{-2} nm^{-1}, being consistent with the value of 3.0×10^{-2} nm^{-1} predicted by the liberalized theory of SD by Cahn, Hilliard, Cook, and deGennes[6,20,21] (**conclusion 2**), to 5×10^{-4} nm^{-1} over the four orders of magnitude of time covered in our experiment, corresponding to the change in $\Lambda_m(t)$ from about 200 nm to 12 μm. Exponents α and β in the power-law analyses

$$q_m(t) \sim t^{-\alpha},\ I_m(t) \sim t^{-\beta} \quad (23)$$

change with t (e.g., from $\alpha \cong 0$ in the early stage to 0.212–1/3 in the intermediate stage and finally to 0.8 in the long time limit of our experiment). The value of exponent α, being greater than 1/3, definitely indicates that the hydrodynamic term makes an important contribution to the dynamic evolution of the self-organized structure (**conclusion 3**), although our system does not reach yet the full hydrodynamic limit ($\alpha = 1$). Time $t_{cr,1}$ in Figure 7 denotes the crossover time from the intermediate stage to the late stage [β is equal to 3α simply because $\langle\Delta\phi(t)^2\rangle$ becomes constant and hence $I_m(t) \sim q_m(t)^3$],[5] whereas time $t_{cr,2}$ is the crossover time from late stage 1 and late stage 2, as will be discussed later. Because the global structure developed in this system is large, the time-resolved LS method plays a major role in the research in this regime, although time-resolved SANS studies are indispensable for the studies in the early to intermediate stages of SD.

Figure 8 shows the scaled structure factor $F(x)$ obtained from the LS profiles in the late stage of SD. $F(x)$, which includes SANS profiles, also is presented later in Figures 18 and 19. In the late stage, $F(x)$ at $x \leq 2$ becomes independent of time, and this indicates that the global structure grows with dynamic self-similarity: the shape of the global structure is conserved, and only the length scale $\Lambda_m(t) = 2\pi/q_m(t)$ increases with time (dynamic scaling). This $F(x)$ is relevant to the structure factor for a bicontinuous domain structure (shown later in Fig. 11). An asymptotic form of $F(x)$ changes with x such that

$$F(x) : x^{-7} \text{ (for } x \leq 2) \text{ and } F(x) \sim x^{-4} \text{ (for } x \geq 2) \quad (24)$$

The result shown in Figure 8 implies that the crossover value of x defined by x_c is given by

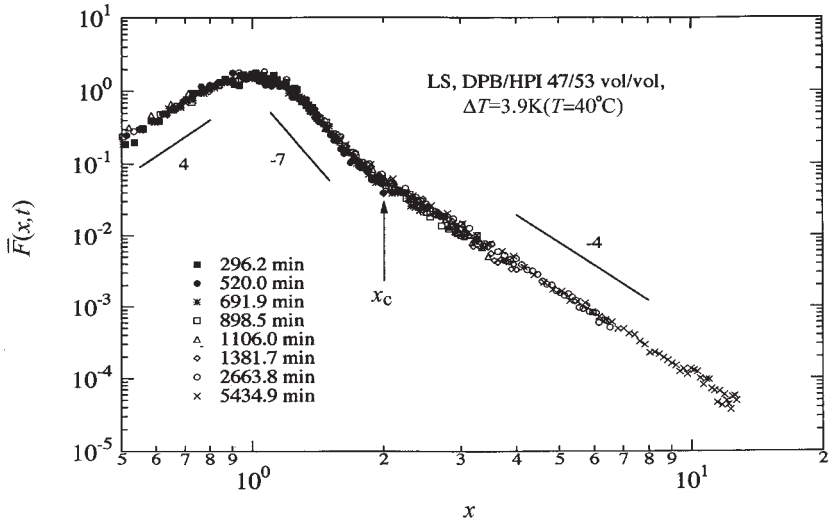

Figure 8. $\overline{F}(x,t)$ obtained from the late-stage LS profiles for the same sample used for Figures 4–7 [$x_c \equiv H(t)/q_m(t) \cong 2$ (independently of time)]. $\overline{F}(x,t)$ will be defined later by eqs. 34 and 43a. The data are based on ref. 26.

$$x_c \equiv H(t)/q_m(t) \cong 2 \tag{25}$$

where $H(t)$ is the crossover q value at time t in the late stage of SD at which the asymptotic behavior changes, as shown by eq 24. It also reveals that the dynamic changes of $H(t)$ and $q_m(t)$ with t are self-similar and are given by the same power law, with the ratio kept around 2 independently of time (**conclusion 4**).

Polymers versus Small Molecules

How does information obtained here for this polymer system compare with that obtained for small-molecule systems? How universal are the results? Figure 9 shows the time evolution of LS profiles during phase separation for critical mixtures of simple liquids of 2,6-lutidine (L) and water (W) (L/W) reported by Chou and Goldburg,[32] one of the famous experimental results in the field of critical phenomena. Very near the critical point, that is, at the temperature lower than the critical point by only 0.6 mK, phase separation occurs at a large length scale and a sufficiently slow temporal scale as discussed earlier so that we can follow the process through time changes in the LS profiles from 10 to 500 s. As the phase-separating structure grows and its Λ_m value grows with t, the magnitude of the scattering vector ($q_m = 2\pi/\Lambda_m$) at the maximum scattering intensity decreases, as shown in Figure 9(a). If the length scale changes but the shape of the structure is kept unchanged in the phase-separation process, the scattering functions at various t values [Fig. 9(a)] can be scaled with length scale Λ_m or wave number q_m. The structure factor scaled with $q_m(t)$ should then become universal with time t. Actually, the scaled structure factor becomes universal with time t, as shown in Figure 9(b). This universal scaled structure factor characterizes the shape of the structure growing with dynamic self-similarity. This is typically found in the late-stage SD process, during which each of the coexisting domains attains the equilibrium composition in the system.

The universal structure factor has also been obtained with the DPB/HPI mixture, as already shown in Figure 8. However, there are differences in the time scales and in the quench depths involved in these two systems. Both factors are greater in the polymer system than in the small-molecule system by approximately 1000 times. Figure 10 compares these two scaled structures.[10] The red line and yellow line are those obtained by Chou and Goldburg[32] and Wong and Knobler,[33,34] respectively, for simple-liquid mixture of I/W where I designates isobutyric acid; the green line is for L/W,[32] and the profile shown by plus signs is for a 50/50 (v/v) mixture of polybutadiene (PB) and polyisoprene (PI). The polymer mixture are described in detail elsewhere.[10] The scaled structure factor for this mixture is identical to that shown in Figure 8. The solid black line was ob-

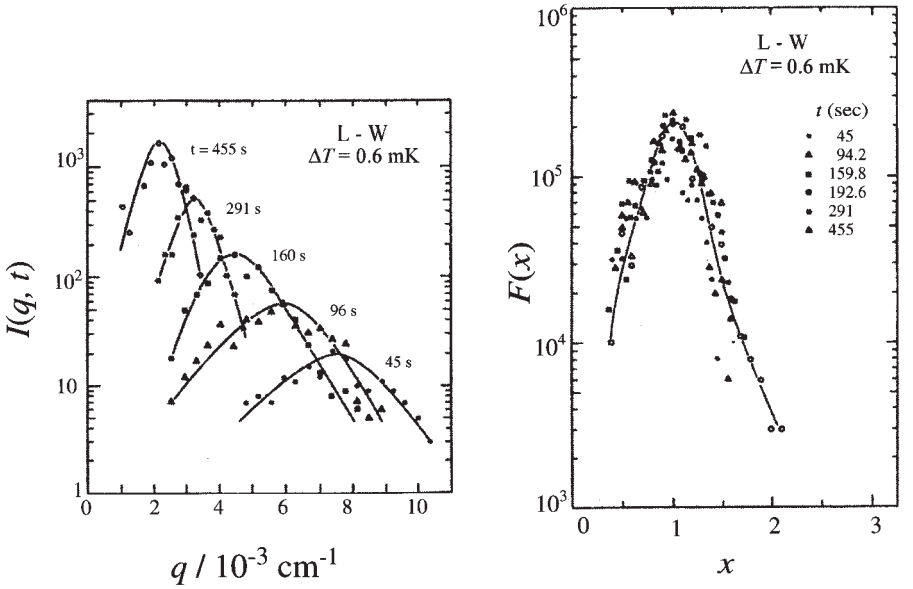

Figure 9. Time evolution of LS profiles: (a) $I(q,t)$ in the late stage of SD for a critical L/W mixture and (b) $F(x)$ (the data are based on ref. 32).

tained from a 3D computer simulation based on the generalized TDGL equation, which takes into account the hydrodynamic interactions[24] (a general nonlinear time-evolution equation). From these results, we can conclude that the growing structures for the simple-liquid mixtures and the polymer mixture have the same shape, although the length scales and time scales for the self-organizing structures are very different in these two systems. We can further conclude that these structures can be theoretically predicted very well by the generalized TDGL equation. The structure factor for the polymer mixture is obtained over a much wider reduced q range (up to ca. 10) than the q range for the simple-liquid mixtures (up to ca. 2). Thus, we can explore further details of phase-separating structures, especially hierarchical structures, with polymers as a model system, as will be detailed later in this section.

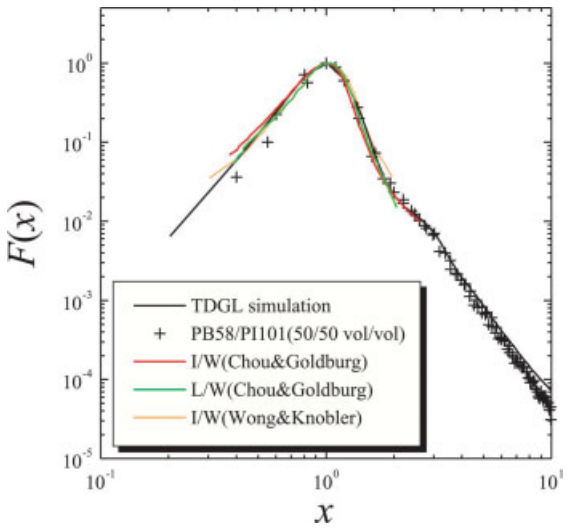

Figure 10. Comparison of $F(x)$ values obtained for critical mixtures of simple liquids [I/W (the red-line data are based on ref. 32, and the yellow-line data are based on ref. 34) and L/W (the data are based on ref. 32], a polymer mixture (50/50 v/v PB/PI), and a 3D simulation based on the generalized TDGL equation with a system size of 128^3 (the data are based on ref. 10).

Visualization of the Universal Structure

What is the real-space structure corresponding to the universal scaled structure factor shown in Figure 10? A 3D phase-separating structure can be detected by laser scanning confocal microscopy (LSCM) for polymer mixtures because the rate of phase separation is much slower than the data acquisition rate of LSCM for constructing the 3D volume objects shown in Figure 11 (~6 min), although quantitative detection is almost impossible for simple-liquid mixtures. Figure 11 presents typical 3D structures constructed with LSCM that were obtained at particular times in the late stage of SD for a binary polymer mixture of DPB and PB-AN with equal phase volumes.[35] The

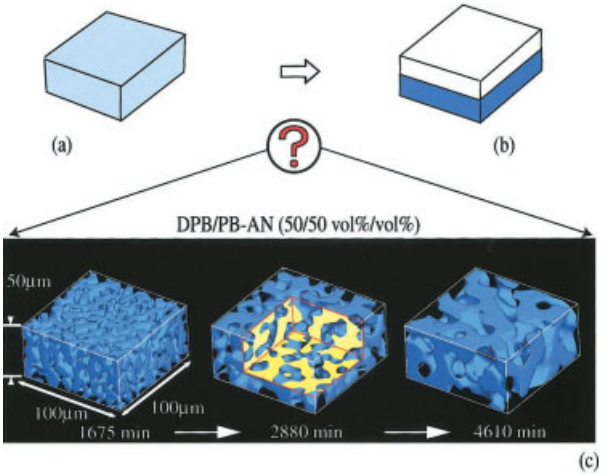

Figure 11. Time evolution of 3D real-space structures, for a critical mixture of polymers in the late stage of SD, constructed with LSCM (part c). Parts a and b schematically show the initial homogeneous mixture before phase separation and the final equilibrium structure after phase separation, respectively. The polymers were DPB and PB-AN. The data are based on ref. 35.

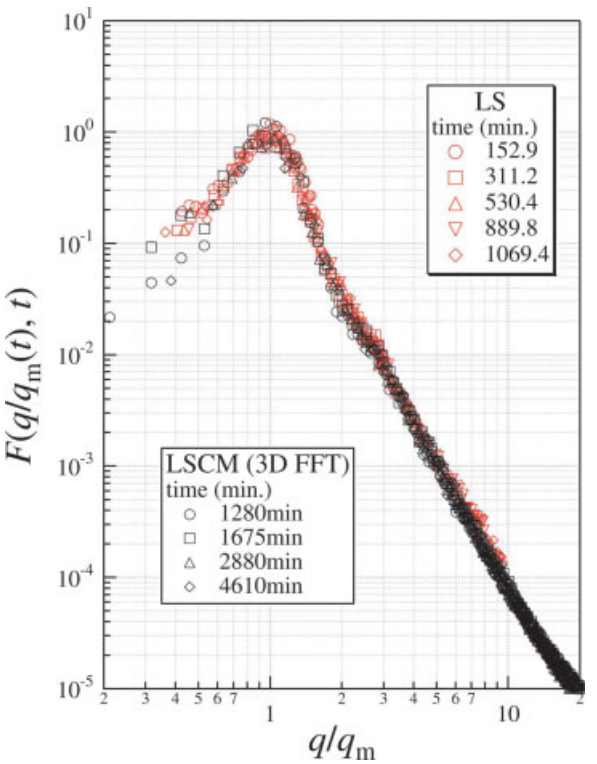

Figure 12. Comparison of $F[q/q_m(t),t]$ values obtained from time-resolved LS and from FFT (Fast Fourier Transform) of 3D real-space structures constructed with time-resolved LSCM for DPB/PB-AN. The data are based on ref. 11.

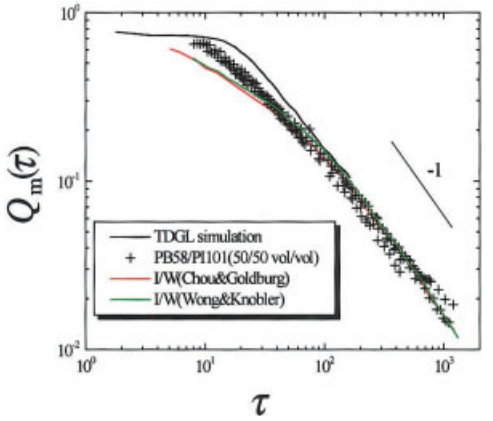

Figure 13. Comparison of the time evolution of $Q_m(\tau)$ versus τ for critical simple-liquid mixtures (I/W), polymer mixtures (50/50 v/v PB/PI), and a 3D TDGL simulation with a system size of 128^3. The data are based on ref. 10.

weight-average molecular weight (M_w) and heterogeneity index (M_w/M_n) of DPB were 1.43×10^5 and 1.12, respectively, whereas the corresponding quantities of PB-AN were 9.5×10^4 and 1.07. M_n denotes the number-average molecular weight. PB-AN is PB labeled with a small amount of anthracene for contrast enhancement under the fluorescence mode of LSCM. The mixture had a critical composition of 46 vol % DPB and a critical temperature of 110 °C, and isothermal SD was carried out at 40 °C. This mixture has various advantages: (1) it satisfactorily fulfills dynamic symmetry (having the parameter $\alpha_a = 0.4$); (2) it has a weak LS contrast arising from a small refractive-index difference because of an isotope effect, so that the large phase-separated structure in the late stage of SD will not cause significant multiple scattering effects; and (3) it has a clear contrast difference between the two phases under LSCM in the fluorescence mode. The small value of α_a becomes really immaterial for our discussion here because the time scale involved is much longer than τ_{ve} and is in the hydrodynamic limit.

The two phases shown in Figure 11 consist of the PB-AN-rich phase colored by blue (reflecting fluorescence light emitted from anthracene) and the DPB-rich phase left empty. The two phases are periodic and cocontinuous, as highlighted by the cross-sectional images displaced in the three orthogonal sections (in the middle image of part c). This kind of structure is called spongelike in the field of differential geometry.[36] Figure 12 presents a comparison of the scaled structure factors obtained by time-resolved LS experiments (shown

by red markers) and by the time-resolved LSCM experiments (shown by black markers); the latter was obtained by a 3D Fourier transform of the real-space images shown in Figure 11. The complete agreement of the two scaled structure factors over a wide q scale and intensity scale ensures that the 3D structures captured here represent the real structures developed in the mixture. Moreover, this structure factor is identical to the universal structure factor shown in Figure 10. Therefore, it must represent those evolved in the late stage of SD for the critical mixtures of simple liquids as well, although real-space 3D images of this kind have never been captured for small molecules, simply because the phase separation is too fast.

The distribution of the interface curvature and its time evolution were analyzed from the 3D real-space structures constructed on the basis of the LSCM experimental results and by 3D computer simulations with the generalized TDGL equation.[37] The results are in very good agreement, revealing that the interface is saddle-shaped almost everywhere, having a negative Gaussian curvature K defined by

$$K \equiv k_1 k_2 \tag{26}$$

where k_i ($i = 1$ or 2) is a principal curvature of the interface. It is essential for the cocontinuous structure to have a saddle-shaped interface because the spaces on both sides of the saddle interface can be continuous, unlike an ellipsoidal interface, for which the space inside the interface is isolated from the space outside the interface.

Further Conclusions and Remarks

Before closing this section, let us summarize the various conclusions obtained by LS, SAXS, and SANS studies, although more details may be found elsewhere.[5]

The time evolution of characteristic wave numbers at various ΔT's [$q_m(t;\Delta T)$] becomes universal with ΔT if we properly scale $q_m(t;\Delta T)$ and t with the difference in the space-time scale of various mixtures undergoing phase separation at different ΔT's [$\xi_c(\Delta T)$ and $t_c(\Delta T)$]. This is the so-called scaling postulate.[38,39] The scaled characteristic wave number [$Q_m(\tau)$] and scaled characteristic time (τ) are given by

$$Q_m(\tau) \equiv q_m(t;\ \Delta T)/q_m(0;\ \Delta T),\ \tau \equiv t/t_c(\Delta T) \tag{27}$$

where $t_c(\Delta T)$ is given by

$$t_c(\Delta T) = 1/[D_{app}(\Delta T) q_m^2(0;\ \Delta T)] \tag{28}$$

$D_{app}(\Delta T)$ is the mutual diffusion coefficient, and $q_m(0;\Delta T)$ is the characteristic wave number, which can be determined from scattering experiments in the early stage of SD when the CHC linearized theory is approximately valid. $q_m(0;\ \Delta T)$ is related to $\xi_c(\Delta T)$ by $q_m(0;\ \Delta T) = 1/(\sqrt{2}\ \xi_c(\Delta T))$. If the scaling postulate is valid, $Q_m(\tau)$ versus τ becomes universal with ΔT, and this means that ΔT changes the space-time scale but not the phase-separation mechanism and process. Good examples showing the validity of the scaling postulate over wide Q_m and τ scales can be found in refs. 40 and 41, for example. Figure 13 shows a test of the scaling postulate for the systems described earlier in conjunction with Figure 10. The behavior of Q_m versus τ is universal, being independent of the systems at least qualitatively. The details are reported elsewhere.[10]

The hydrodynamic interactions play an important role in the domain growth in the late stage of SD, so that the following scaling law

$$Q_m \sim \tau^{-\alpha},\ \alpha = 1 \tag{29}$$

is fulfilled, as shown in Figure 13. The generalized TDGL equation, expressed by reduced variables, contains a single system-dependent parameter[42] $\tilde{\eta}$ which is a reduced viscosity:

$$\tilde{\eta} = \frac{1}{45}\left(\frac{N}{2N_e}\right)^{1.4} \text{ for } N > N_e \tag{30}$$

For critical simple-liquid mixtures, $\tilde{\eta}$ is a universal quantity ($\tilde{\eta} \cong 0.12$), and so Q_m versus τ becomes a universal curve. This is also the case for polymer mixtures with $N < N_e$. However, for polymer mixtures with $N > N_e$, $\tilde{\eta}$ is not a universal constant but depends on N/N_e, so that Q_m versus τ also becomes nonuniversal. Systems with different N/N_e values show branching in the curve of log Q_m versus log τ (so-called N-branching[40]) because the larger N/N_e is, the larger $\tilde{\eta}$ is and the later the hydrodynamic interactions come into play. Therefore, to obtain the universal curve for entangled polymer systems, we must use the reduced time (τ_p) renormalized by N/N_e, instead of τ itself,

$$\tau_p \equiv \tau(N/N_e)^{1.4} \tag{31}$$

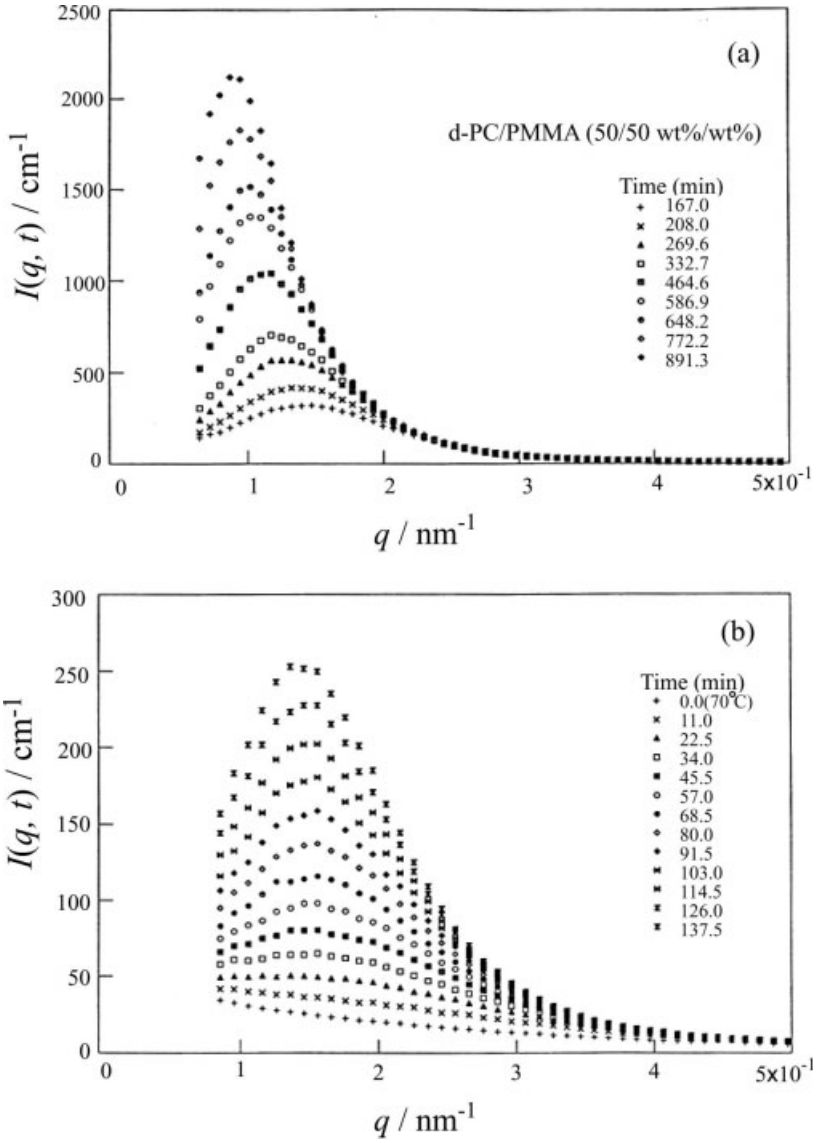

Figure 14. Time evolution of the SANS profiles of a 50/50 (w/w) mixture of deuterated polycarbonate (d-PC) and poly(methyl methacrylate) (PMMA) in the very early (0–45.5 min), early (57.0–208 min), and intermediate-to-late stages ($t > 269.6$ min) of SD (from ref. 45).

as theoretically predicted first by Onuki[43] and experimentally elaborated by Hashimoto and coworkers.[40,44] In fact, the polymer mixture shown in Figure 13 still does not show the scaling relation of eq 29 but rather shows the exponent $\alpha \cong 0.85$ in eq 23, and thus it is likely that the system is asymptotically approaching a time domain in which eq 29 is fulfilled.

Polymer mixtures definitely show the early-stage SD regime in which this characteristic behavior can be described by Cahn's linearized theory; for example, $q_m(t)$ is a constant independent of time over a large time scale t or a reduced timescale[5] $\tau \lesssim 1$. In the time-resolved SANS experiment[45] shown in Figure 14, for example, the early stage of SD can be observed in the time scale of $45.5 \lesssim t \lesssim 208$ min or $0.38 \sim \tau \lesssim 1.7$. The change in the scattering structure factor at $t < 45.5$ min represents the very early stage during which the characteristic Fourier mode of the composition fluctuation having $q_m(0)$ ($\cong 1.4 \times 10^{-1}$ nm^{-1}) becomes dominant, whereas that at $t > 208$ min represents the intermediate stage of SD in which q_m starts to decrease because the mode-

coupling effects arising from the nonlinearity in the time-evolution process.

The universal scaled structure factor in the late stage of SD was for the first time elucidated to reflect the spongelike structure both for polymers and for simple liquids.[10]

Global-to-Asymptotic Crossover Regime

Upon reducing the length scale of our observation such that $r < R_m$, we come to the asymptotic or interface (Porod's law) regime. However, before discussing this regime, let us add a brief remark about the global-to-asymptotic crossover regime in which our q scale of observation is $(1/\Lambda_m) < q < (1/R_m)$. In this regime, scattering is affected by a special curvature of the interface, which may be called the scattering-mean curvature. The effect of the interface curvature on the scattering was elaborated first by Kirste and Porod[46] and later by Tomita.[47] They found the following asymptotic behavior for the scattered intensity $[I(q)]$ and the density correlation function $[\gamma(r)]$:

$$\bar{I}(q) = \frac{\Sigma}{\pi X(1-X)}\, q^{-4}\left(1 + \frac{1}{R_m^2}\, q^{-2} + \cdots\right) \qquad (32)$$

and

$$\gamma(r) = 1 - \frac{\Sigma}{4X(1-X)}\, r\left(1 - \frac{1}{12R_m^2}\, r^2 + \cdots\right) \qquad (33)$$

where $\bar{I}(q)$ is defined by

$$\bar{I}(q) \equiv I(q) \Big/ \int_0^\infty q^2 I(q)\, dq \qquad (34)$$

and X is the volume fraction of one of two phases. The scattering-mean curvature (R_m^{-1}) is defined as follows:

$$R_m^{-2} \equiv [3\langle H^2\rangle - \langle K\rangle]/2 \qquad (35)$$

where the quantity $\langle I\rangle$ ($I = H^2$ or K) is an area-averaged quantity of I defined by

$$\langle I\rangle = \int I\, da \Big/ \int da \qquad (36)$$

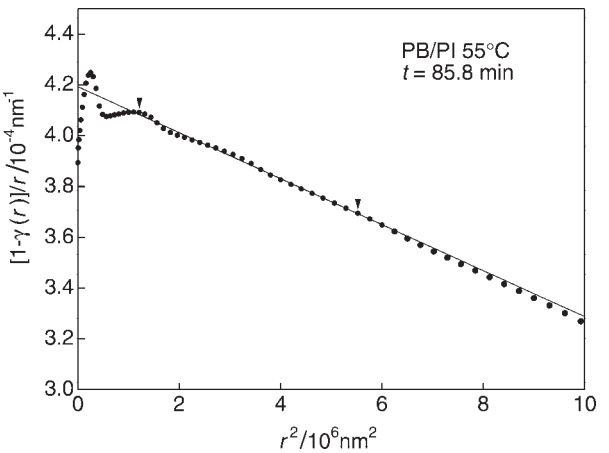

Figure 15. Plot determining the scattering-mean curvature of the interface for the PB/PI mixture in the late stage of SD (from ref. 49).

$\int da$ is the integral over the entire interface area, K is the local Gaussian curvature of the interface defined by eq 26, and H is the local mean curvature defined by

$$H \equiv (k_1 + k_2)/2 \qquad (37)$$

For $qR_m \gg 1$ or $r/R_m \ll 1$, the second term in rhs of eq 32 and the third term in rhs of eq 33 vanish, and hence the equations are reduced to Porod's law.[48] However, when qR_m and r/R_m approach unity from a larger value of q and a smaller value of r, respectively, the curvature gives an upward deviation from Porod's law in the plots of both $I(q)$ versus q and $\gamma(r)$ versus r, which may be used to estimate R_m. Figure 15 presents a typical plot of $[1 - \gamma(r)]/r$ versus r^2 obtained from LS for a particular polymer mixture of PB and PI with a composition close to the critical one at a particular time (85.8 min) and temperature (55 °C) in the late stage of SD.[49] The slope and intercept at $r^2 = 0$ in the plot yield $R_m^{-1} = 5.21 \times 10^{-4}$. How does this value compare with the value obtained from the real-space analysis? Unfortunately, there are no real-space data available for this system. Thus, we compare the real-space results obtained for another polymer mixture of PB and poly(styrene-*random*-butadiene) (SBR).[50] To facilitate the comparison, we compare the scattering-mean curvature reduced by the characteristic wave number $[q_m(t)]$ defined by the following dimensionless quantity (C_r):

$$C_r \equiv R_m^{-1}(t)/q_m(t) \qquad (38)$$

The measured value of $q_m(t) = 1.0 \times 10^{-3}$ nm^{-1} for the PB/PI system yields $C_r = 0.52$, which is defined as C_{rS} to designate the C_r value estimated by the scattering method. The phase-separated structure of PB/SBR at 100 °C for 7 h in the late stage of SD was analyzed by LSCM to obtain the curvature distribution $[P(H,K)]$.[51] The results yield $q_m = 0.52 \times 10^{-3}$ nm^{-1}, $\langle H^2 \rangle = 2.2 \times 10^{-8}$ nm^{-2}, and $\langle K \rangle = -6.2 \times 10^{-8}$ nm^{-2}. These values, together with eqs 35 and 38, give the value of C_r defined as $C_{rL} = 0.49$. C_{rS} and C_{rL} agree quite well ($C_{rS}/C_{rL} = 1.1$). These results ($C_r = C_{rS} = C_{rL} \cong 1/2$) and the result $H(t)/q_m(t) \cong 2$ give an approximation of the relation between the crossover q value of $H(t)$ and R_m^{-1}:

$$H(t) = 4R_m(t)^{-1} \tag{39}$$

This provides a quick and rough estimation of the scattering-mean curvature for the sponge-like phase-separated structure from $I(q,t)$ or $F(x)$.

Asymptotic (or Interface) Regime

In this regime, the interface appears to be flat because the q scale or r scale of our observation is large ($q > 1/R_m$) or small ($r < R_m$), respectively. Hence, the second term and third term on rhs of eq 32 and 33, respectively, become insignificant. However, the effect of the finite interface width comes into play in the scattering formula so that the asymptotic form of the scattering $[\bar{I}(q)]$ in eq 32 should be replaced by

$$\bar{I}(q) = [\pi X(1 - X)]^{-1} \Sigma q^{-4} \exp(-\sigma^2 q^2) \tag{40}$$

where σ is the parameter associated with t_I[52] [$t_I = (2\pi)^{1/2}\sigma$]. Equation 40 is Porod's equation generalized for a pseudo two-phase system with a finite interface thickness. $I(q)$ is corrected for the scattering intensity $[I_{thermal,e}(q)]$ arising from thermal composition fluctuations within each of two phases (as discussed later) and for thermal diffuse scattering (TDS) arising from longitudinal acoustic phonons[53].

The validity of the asymptotic form of eq 40 was confirmed experimentally for the LS data in the late stage of SD;[54] Σ and t_I were evaluated as a function of time with plots of $\ell n[q^4 \bar{I}(q)]$ versus q^2. In Figures 8, 10, and 12, $F(x)$ at $x \geq 2$ is represented by $F(x) \sim x^{-n}$, or $I(q)$ at $q \geq H$ is represented by $I(q) \sim q^{-n}$, with n slightly larger than 4 if the ordinate scale is expanded. However, it appears that $n = 4$ for the compressed scale used in these figures. That n is greater than 4 and that the asymptotic form of eq 40 is valid lead us to the following conclusions. The interface observed at length scale r at $t_I < r < R_m$ is flat but has a diffuse boundary, and so the scattering contrast varies gradually across the interface. Consequently, the interface at a given time in the late stage is not characteristic of the fractal surface (**conclusion 5**). If it is characteristic of a fractal surface, exponent n should satisfy $3 \leq n \leq 4$ because

$$n = 2d - d_s \tag{41}$$

where d and d_s are the space dimensionality ($d = 3$ for 3D space) and the surface fractal dimension, respectively.

Figure 16 shows the time changes in $\Sigma(t)$, $t_I(t)$, and $\Sigma(t)/q_m(t)$ in the late stage of SD, which were estimated on the basis of eq 40 for the same DPB/HPI mixture used for Figures 4–8.[26] $\Sigma(t)$ naturally decreases with time because of the interfacial tension and is given by a power law

$$\Sigma(t) \sim t^{-\gamma_I} \tag{42}$$

with $\gamma_I \cong 0.8$, so that the time evolution of the interface has dynamic self-similarity; that is, it is dynamically fractal (**conclusion 6**), as schematically shown in Figure 17. A close observation indicates that γ_I is slightly larger than the scaling exponent α defined by eq 23 at $t_{cr,1} < t < t_{cr,2}$ and that γ_I is equal to α at $t > t_{cr,2}$, as revealed from the time change in Σ/q_m. The inequality $\gamma_I > \alpha$ suggests that the local structure with a higher $q(\cong\Sigma)$ values relaxes more quickly toward equilibrium than the global structure with a smaller $q(\cong q_m)$ values. This is consistent with conclusion 1 and provides a reason why the interface at a given time in the late stage does not have surface fractality (conclusion 5). The characteristic interface thickness in the late stage covered in our experiment tends to decrease with time from about 200 nm to the equilibrium value t_{Ie} of about 80 nm, which is shown by the solid line at the time scale longer than the same crossover time $t_{cr,2}$ between late stages 1 and 2 (**conclusion 7a**). t_{Ie} is consistent with the value predicted by the Joanny–Leibler theory[55] (**conclusion 7b**).

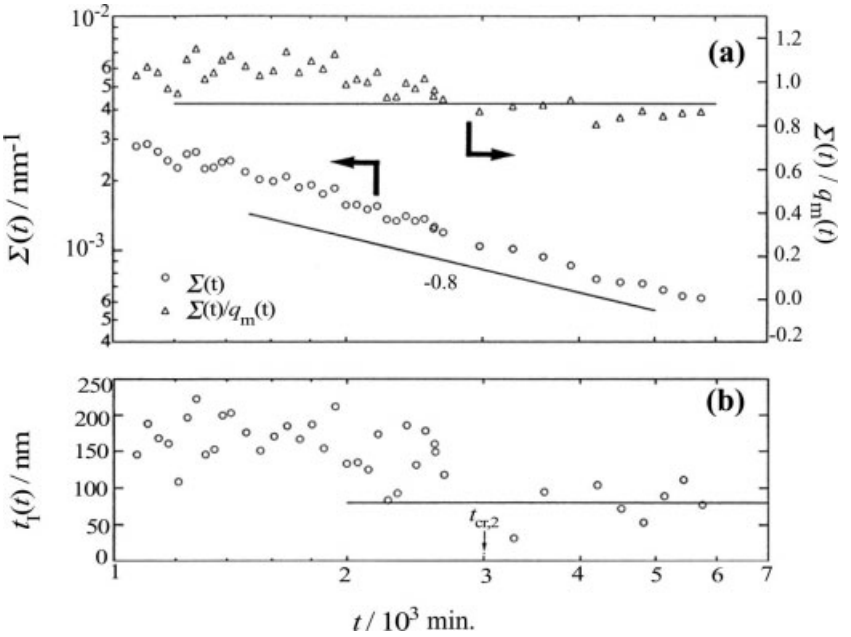

Figure 16. Time changes of Σ, Σ/q_{m}, and t_{I} obtained from the LS profiles in the asymptotic regime and in the late stage of SD for the same DPB/HPI sample used for Figures 4–8 (from ref. 26).

Now let us further explore this regime by investigating the scaled structure factor $\bar{F}(x)$ with q_{m}:

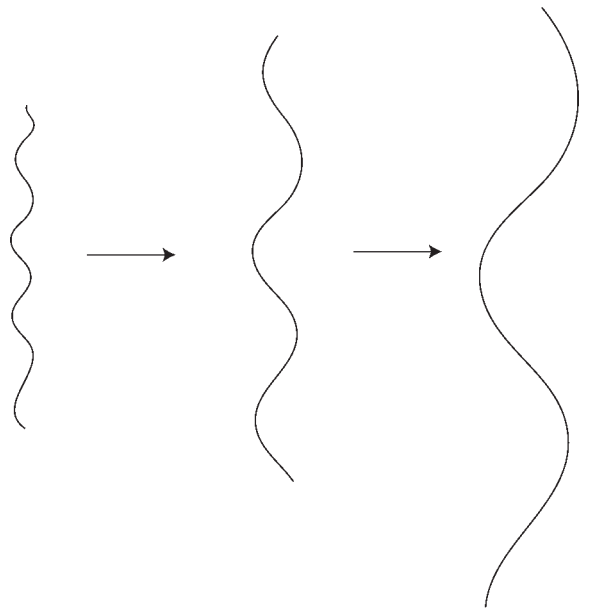

Figure 17. Schematic illustration of dynamic fractality (dynamic self-similarity) in the time evolution of a part of the interface from left to right in the late stage of SD.

$$\bar{F}(x) \equiv \bar{I}(q)q_m^3 \tag{43a}$$

$\bar{I}(q)$ has already been defined by eq 34. From eq 40, $\bar{F}(x)$ in this regime is given by

$$\bar{F}(x) = [\pi X(1-X)]^{-1}(\Sigma/q_m)x^{-4}\exp[-(\sigma q_m)^2x^2] \tag{43b}$$

$\bar{F}(x)$ [or $F(x)$] in this regime involves two length scales: σ and $1/q_{\mathrm{m}} \sim \Lambda_{\mathrm{m}}$. In the later phase of the late stage at $t > t_{\mathrm{cr},2}$, Σ/q_{m} and σ (or t_{I}) reach the respective constant values, as shown in Figure 16. However, q_{m} keeps decreasing with t according to the scaling law of eq 23 or 29, and so does the parameter $\sigma q_m = \sqrt{2\pi}(t_I/\Lambda_m)$ which is related to the relative interfacial thickness. Thus, the exponential factor in rhs of eq 43b gradually increases and approaches unity. Thus, $\bar{F}(x)x^4$ gradually increases toward Porod's limiting value.

Explorations of the aforementioned phenomenon involve the investigation of $\bar{F}(x)$ up to large x values, which badly needs a combined time-resolved SANS and LS technique. The SANS intensity profiles were corrected for $I_{\mathrm{thermal,e}}(q)$. The TDS intensity level is very low in comparison with the intensity level $I_{\mathrm{thermal,e}}(q)$ for this system, and so the TDS correction is not important at

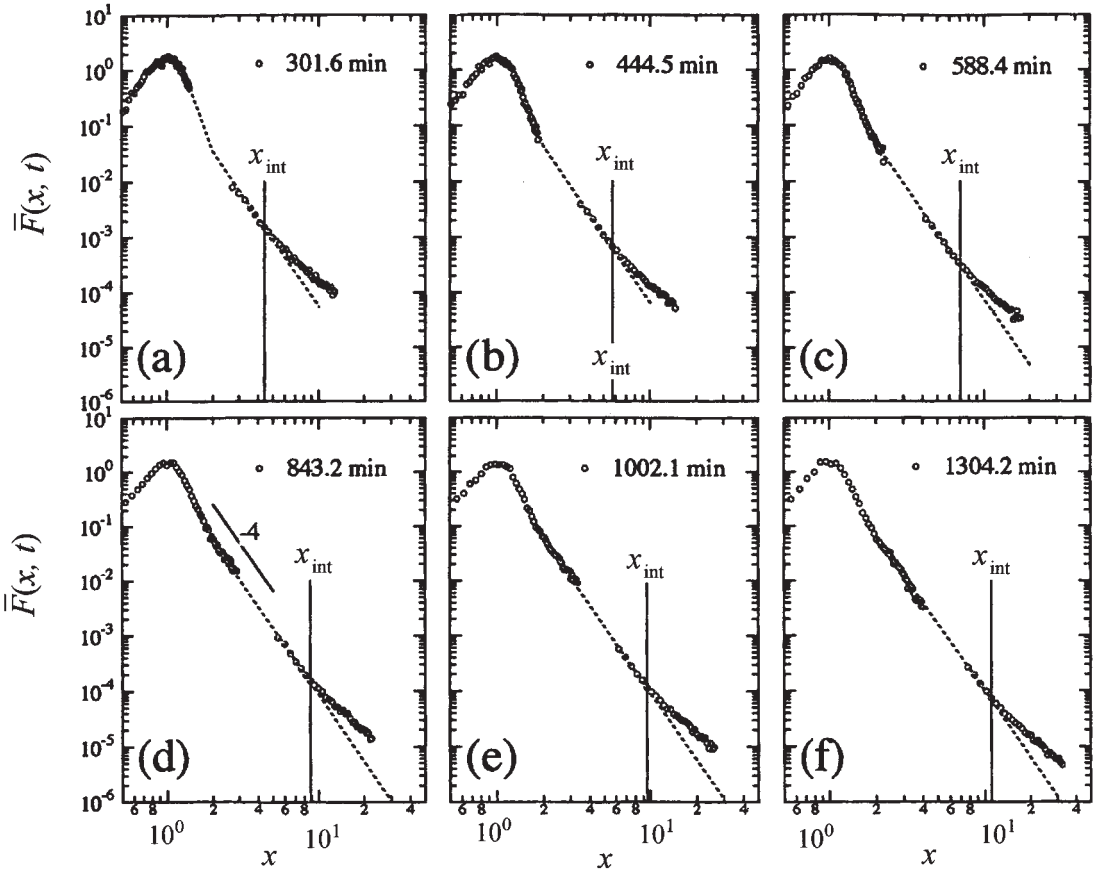

Figure 18. $\bar{F}(x,t)$ at six representative times in the late stage of SD plotted in a double-logarithmic scale for the same DPB/HPI mixture used for Figures 4–8 and 16. The $\bar{F}(x,t)$ values in the q gap, shown as broken lines, are interpolated with the asymptotic laws of $\bar{F}(x,t)$ with x (x^{-7} at $x \leq 2$ and x^{-4} at $x > 2$; from ref. 27).

all. The LS intensity level is much higher than the TDS intensity level and $I_{\text{thermal,e}}(q)$, and so the LS intensity does not need correction at all.

The corrected SANS intensities were then used to construct $\bar{F}(x,t)$ and are plotted in Figure 18 together with those obtained by LS at six representative times[27] in the late stage of SD for the same DPB/PI mixture discussed in Figures 4–8 and 16. The value $F(x)$ in the q gap between LS and SANS was estimated, as shown by the dotted line in each figure, by the interpolation of $\bar{F}(x,t)$ with x^{-7} from the large values of x covered with LS and with x^{-4} from the small values of x covered with SANS. $\bar{F}(x,t)$ in the gap has an x^{-4} dependence in Figure 18(b–f), whereas it has x^{-7} for $x < 2$ and x^{-4} for $x \geq 2$ in Figure 18(a), according to the discussion in the previous section.

Two important features can be observed in Fig 18: (1) all $\bar{F}(x,t)$ values at different times have a deviation from q^{-4} (or x^{-4}) at the high q range of $q > q_{\text{int}}$ or x range of $x > x_{\text{int}}$ so that they appear to have a shallower q dependence (close to $q^{-2.5}$) independent of t, and (2) the crossover wave number q_{int} or reduced wave number $x_{\text{int}} \equiv q_{\text{int}}/q$ is a function of t, so that x_{int} increases with t. So far, much attention has been focused on $\bar{F}(x,t)$, only at relatively small x values satisfying $x \leq 2$, to characterize the global structure, but not much attention has been paid to $\bar{F}(x,t)$ at $x > 2$, which characterizes the Fourier modes of the structure occurring at shorter length scales, except for a few works.[5,26,54] Such a wide range of x as covered in this work, as large as 30, has never been reported. Features 1 and 2 have never been observed, a qualitative picture of which is presented later.

Figure 19 compares curves of $\bar{F}(x,t)$ like those shown in Figure 18 at three representative t's (227.8, 444.5, and 1002.3 min, corresponding to profiles 1–3).[27] Profile 4, plotted with cross mark-

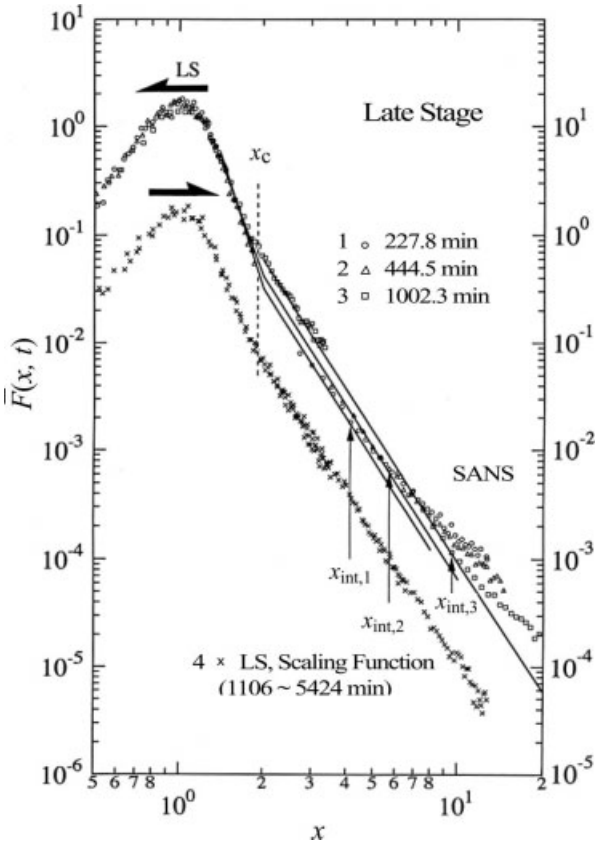

Figure 19. $\bar{F}(x,t)$ for the late stage of SD plotted in a double-logarithmic scale for the same sample used for Figure 18. Profiles 1–3 are the LS and SANS profiles for $\bar{F}(x,t)$ obtained in the late stage at 227.8, 444.5, and 1002.3 min after the onset of SD, whereas profile 4 is the LS profile obtained between 1106 and 5424 min. The solid lines in the profiles have been estimated by the asymptotic law described in Figure 18., and the intensity level at $x > 2$ increases from profile 1 to profile 3 (from ref. 27).

ers, is $\bar{F}(x,t)$ obtained by LS at much later times (1106–5424 min) during which $\bar{F}(x,t)$ is universal with t, even at $x \geq 2$ (but at $x \leq x_{int}$, x_{int} for this profile existing beyond the highest x limit accessible to this experiment). Profile 4 has been vertically shifted by 1 decade for clarity. In profiles 1–3, the LS and SANS profiles have been combined just as in Figure 18. The q gap for each profile has been estimated in the same manner as described previously.

We can find two kinds of nonuniversalities in Figure 19. The first nonuniversality, called *extrinsic nonuniversality*, is that in the Porod region, in which $\bar{F}(x,t)$ is approximately x^{-4} the intensity of $\bar{F}(x,t)$ increases with t. This extrinsic nonuniversality primarily arises from a decreasing contribution of the interface thickness in $\bar{F}(x,t)$, as discussed previously in detail in conjunction with eq 43b. This nonuniversality appears in late stage I and disappears in late stage II: $\bar{F}(x,t)$ eventually becomes universal when $t_I/\Lambda_m(t)$ approaches 0. This is clearly shown by the fact that profile 4, which corresponds to $\bar{F}(x,t)$ in late stage II, falls onto $\bar{F}(x,t)$ at 1002.3 min (profile 3) at $x < x_{int,3}$. Thus, the nonuniversality is a result of the existence of the two length parameters $\Lambda_m(t)$ and $t_I(t)$, which characterize the system, and the contribution of $t_I(t)$ is not trivial at particular q and t domains.

The second nonuniversality, called *intrinsic nonuniversality*, can be observed at $x \geq x_{int,i}$ (i = 1–3 in Fig. 19). Thus, even in the later time of the late stage (i.e., late stage II), the intrinsic nonuniversality appears as x crosses over $x_{int,i}$. The scattering intensity from the interface, which decreases according to x^{-4}, becomes very weak at large x values greater than x_{int}. Therefore, the intensity at large x values is eventually outweighed by the intensity arising from the composition fluctuations inside the interphase or inside each domain. Because the intensity arising from the fluctuations within each domain [$I_{thermal,e}(q)$] has already been subtracted from $I(q,t)$, the remaining contribution to $\bar{F}(x,t)$ in the large x region should be excess scattering from the interphase. Thus, in the high x range above $x_{int,i}$ (i = 1 − 3), $\bar{F}(x,t)$ becomes related to that for the interphase. To the best of our knowledge, this intrinsic nonuniversality has never been reported in the past. We find $\bar{F}(x,t) \sim x^{-n}$, with $n \cong 2.5$ independent of t at $x > x_{int}$, as discussed in the next section. The crossover value x_{int} increases with time because the reduction of $q_m(t)$ with t outweighs that of the crossover wave number [$q_{int}(t)$]. The existence of x_{int} reflects the fact that an additional characteristic length scale ξ_{int} plays an important role in the scattering at $q > q_{int}$.

Interphase Regime

As shown in Figures 5 and 6, the scattering in this regime ($1/t_I < q < 1/R_g$ or $R_g < r < t_I$) becomes time-independent in the late stage of SD. However, the intensity level in this regime is definitely higher than $I_{thermal,e}(q)$ at 40 °C, as highlighted by the hatching in Figures 5 and 6 (**conclusion 8a**). The results are reproducible, and the excess scattering in this q region cannot be observed for the scattering profiles for the single-

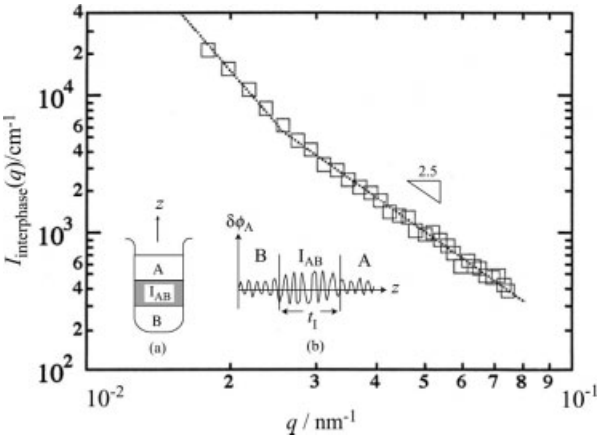

Figure 20. Excess SANS scattering intensity profile [$I_{\text{interphase}}(q)$] from composition fluctuations in the interphase for the same DPB/PI mixture used for Figures 4–8, 16, 18, and 19 in the late stage of SD. Inset (a) represents a macroscopic phase separation in two phases (A and B) with an interphase (I_{AB}), whereas inset (b) schematically represents composition fluctuations in A and B and in I_{AB} of characteristic thickness t_I.

phase regions or for those in the early to intermediate stages of SD.

As shown in Figure 6, the scattering dominantly arises from the interface in the high q region satisfying $q > 1/R_m$; Σ and t_I are relevant parameters characterizing our system. However, its intensity becomes insignificantly small in the interphase regime because the intensity decreases according to q^{-4}, and hence it is dominated by the intensity arising from thermal composition fluctuations within coexisting two phases ($I_{\text{thermal,e}}$) and the intensity arising from those within the interphase ($I_{\text{interphase}}$). Because $I_{\text{thermal,e}}$ at 40 °C is well characterized by SANS, as shown by the broken line in Figures 5 and 6, we can approximately estimate the contribution of $I_{\text{interphase}}$:

$$I_{\text{interphase}}(q) \sim I(q) - I_{\text{thermal},e}(q) \qquad (44)$$

$I_{\text{interphase}}(q)$, estimated from eq 44, is plotted in Figure 20 with a double-logarithmic scale. The straight line in the plot has a slope of −2.5:

$$I_{\text{interphase}}(q) \sim q^{-2.5} \qquad (45)$$

This result is analogous to the scattering from the crumpled tethered membrane[56,57] (conclusion 8b). This intriguing phenomenon observed in the late stage of SD has never been reported before and deservers further investigation in the future.

The scattering observed with this wave-number scale provides a simple picture, as presented in the insets (a) and (b) in Figure 20. SANS in this regime detects thermal equilibrium structures of the two phases A and B as well as the intervening interphase I_{AB}, as shown in the inset (a) in Figure 20. The interfacial area Σ and volume Σt_I, as well as the composition difference $\Delta\Phi^e$ between the two phases and the average composition gradient at the interface, are not relevant parameters here, but the fluctuations from the average composition profile within the interphase are relevant. If we can scan the relevant fluctuations normal to the interface (z axis), we can anticipate the fluctuations of component A ($\delta\phi_A$), as depicted in the inset (b) in Figure 20. $\delta\phi_A$ in the A and B phases is predicted from $I_{\text{thermal,e}}$ and is relatively small in comparison with $\delta\phi_A$ in the interphase. The latter is expected to increase with scanning from the edges of the interphase toward the middle, as the system locally becomes effectively close to the critical condition. The fluctuations are anticipated to be directionally dependent; $\delta\phi_A$ parallel to the interface may be different from that perpendicular to the interface. Theoretical and experimental studies of the fluctuations deserve future investigation.

Finally, the compositions fluctuations in the interphase are expected to be damped as t_I decreases. Hence, $I_{\text{interphase}}(q)$ cannot be observed, and ξ_{int} will not come into play in a strong segregation condition.

Local Regime

In this local regime, the length scale of observation ($r < R_g$ or $q > 1/R_g$) is so small that the scattering depends only on the local composition [$\phi_A(t)$]. $\phi_A(t)$ increasingly deviates from the initial composition (ϕ_A^0) with time after the onset of SD. The deviation increases with time in the early to intermediate stages and reaches the equilibrium at the end of the intermediate stage or the beginning of the late stage. This scattering from thermally activated local thermal composition fluctuations inside each domain [$I_{\text{thermal}}(q,t)$] is given at $q > \xi_T$ by

$$I_{\text{thermal}}(q, t) \sim \langle \phi_A(t)[1 - \phi_A(t)] \rangle_{\text{space}} q^{-2} \qquad (46)$$

where $\langle x \rangle_{\text{space}}$ is the average of quantity x over all space. It changes from

$$I^{23^\circ C}_{\text{thermal},e}(q) \sim \phi^0_A(1-\phi^0_A)q^{-2} \quad (47)$$

at 23 °C before the onset of SD to

$$I^{40^\circ C}_{\text{thermal},e}(q) = \{X[\phi^e_{A1}(1-\phi^e_{A1})] + (1-X)]\phi^e_{A2}[1-\phi^e_{A2}]\}q^{-2} \quad (48)$$

at the beginning of the late-stage SD process when the local composition of the phase-separating domains attains the equilibrium composition shown in Figure 4. For $\phi^0_A \cong 1/2$, as in our case, $I_{\text{thermal}}(q,t)$ decreases from the level shown by the solid line to that by the broken line in the lower half of Figure 5. We can estimate the time evolution of the composition difference $[\Delta\Phi(t)]$ defined in Figure 4 from that of $I_{\text{thermal}}(q,t)$. The estimation yielded such a natural result[29] that $\Delta\Phi(t)$ increases with t and reaches the equilibrium value ($\Delta\Phi^e$) at $t \geq t_{cr,1}$ in the late stage of SD, as given by eq 49a (**conclusion 9a**). Here $t_{cr,1}$ was determined from the time scale when the scaling exponents α and β in eq 23 satisfy $\beta = 3\alpha$ and when $F(x,t)$ versus x becomes independent of time. The deviation of the composition difference at time t $[\delta\Delta\Phi(t)]$ from $\Delta\Phi^e$, defined in eq 49b, can be approximated by eq 49c in the time domain in which $\Delta\Phi(t)$ is close to $\Delta\Phi^e$:

$$\Delta\Phi(t) = \Delta\Phi^e(t/t_{cr,1})^{1/10} \text{ at } t \leq t_{cr,1} \text{ and } \Delta\Phi^e \text{ at } t > t_{cr,1} \quad (49a)$$

$$\delta\Delta\Phi(t) \equiv \Delta\Phi^e - \Delta\Phi(t) \quad (49b)$$

$$= \Delta\Phi^e \exp(-t/\tau_{cf}) \quad (49c)$$

where τ_{cf} is 100 min at 40 °C. Equation 49c suggests the way in which the system attains equilibrium in terms of $\delta\Delta\Phi(t)$ and that $\delta\Delta\Phi(t)$ can be described by a linear differential equation with t (**conclusion 9b**).

Summary

A number of conclusions (conclusions 1–9) have been elucidated on the space–time organization of the structures in binary critical mixtures via SD with dynamically symmetric polymer mixtures used as model systems. The self-organization of the structures is characterized by at least four independent length scales: (1) $\Lambda_m(t) = 2\pi/q_m(t)$, the characteristic length scale for the global structure; (2) $t_I(t)$, the characteristic interface thickness; (3) ξ_T, the thermal correlation length within each phase-separated domain; and (4) ξ_{int}, the thermal correlation length characterizing thermal composition fluctuations in the interphase. ξ_{int} becomes irrelevant in a strong segregation condition with t_I of the order of segment length a. The mean radius of the interface curvature $[R_m(t)]$ has a special relationship with $\Lambda_m(t)$ (conclusion 4). As for time sequences of various events in the self-organization process, the following points are worth noting: (1) the local composition first reaches the equilibrium one at phase-separation temperature T at $t = t_{cr,1}$, the onset time of the late stage of SD (conclusion 9a); (2) the interfacial thickness subsequently reaches the equilibrium value t^e_I at $t \geq t_{cr,2}$ in the late stage (the late stage II; conclusion 7a); and (3) $\Sigma(t)$ (the local wave number) and $q_m(t)$ (the global wave number) keep decreasing with t, reducing the interfacial free energy of the systems. In the early time in the late stage ($t_{cr,1} \leq t \leq t_{cr,2}$, late stage I), $\Sigma(t)$ relaxes more quickly than $q_m(t)$, and this is consistent with the general law found in the ordering process driven by the interfacial free energy (conclusion 1).

DYNAMICS OF COMPOSITION FLUCTUATIONS IN DYNAMICALLY ASYMMETRIC MIXTURES

We have discussed the nonlinear dynamics encountered in the phase-separation processes for dynamically symmetric mixtures. In the discussion, we have highlighted not only the universal features in the behavior of small-molecule systems and polymer systems but also various pieces of new information unveiled with polymers as model systems and with a combined SANS and LS method to cover an extremely wide q range. In this section, we focus on the dynamics for dynamically asymmetric mixtures. Again, we should stress that polymers provide very good model systems for exploring various unexplored phenomena that underlie the topical system, simply because the dynamic asymmetry parameter α_a can easily be tuned through changes in the relative molecular weights of the mixtures. The effects of the dynamic asymmetry on the dynamics of the fluctuations and pattern formation are generally important for small-molecule systems as well, such as microemulsion systems consisting of a surfactant, oil, and water, membranes, and any

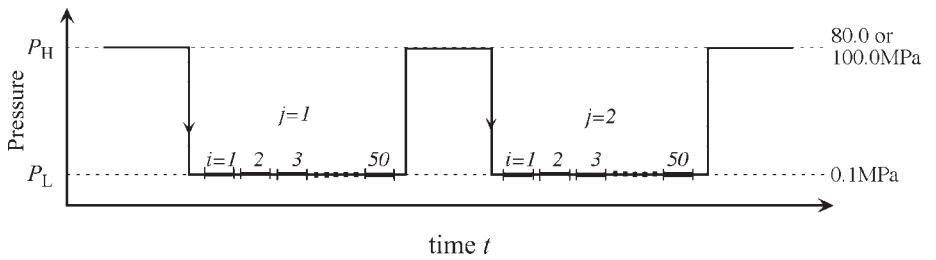

Figure 21. Scheme of a signal-averaging technique used in the SANS relaxation experiments which involve a pressure jump within a single-phase region.

systems having a large mobility difference among the constituent molecules or supramolecules.

Systems to be Handled

Here we are concerned with an asymmetric polymer mixture[19] consisting of DPB ($M_w = 3.74 \times 10^5$) and PI ($M_w = 8.5 \times 10^4$). Their R_g values for the unperturbed chains are 21.0 and 9.5 nm, respectively. The weight-average DPs of DPB and PI (defined as $N_{W,DPB}$ and $N_{W,PI}$, respectively) have a ratio of $N_{W,DPB}/N_{W,PI} = 5.7$, and the self-diffusivities of PI and DPB (defined as $D_{PI} = 3.2 \times 10^{-17}$ m^2/s and $D_{DPB} = 8.1 \times 10^{-19}$ m^2/s, respectively) have a ratio of $D_{PI}/D_{DPB} \cong 40$. Therefore, the system has a sizable asymmetry parameter ($\alpha_a \cong 1.4$).

We explore the dynamics of the composition fluctuations of the mixture with a composition of 50/50 w/w in a single-phase state with a time-resolved SANS technique. To achieve this goal, we explore the relaxation process of the fluctuations after rapid changes in the pressure within a single phase. The results obtained in this study are discussed later in conjunction with those expected or obtained for other systems, such as polymer solutions and aqueous dispersions of ionic colloids.

Signal-Averaging Time-Resolved SANS Technique

When the pressure imposed on the system is suddenly changed from P_H to P_L at a given temperature within a single-phase state, the thermodynamic state of the system changes and hence the composition fluctuations change or relax from those at equilibrium at P_H to those at equilibrium at P_L. The relaxation process can be detected by time-resolved SANS. The relaxation for the DPB/HPI mixture occurs over a time scale of approximately 100 s and should be followed with a time slicing of approximately 10 s or less. The time-sliced SANS profiles obtained with this time scale still have a poor single-to-noise ratio. We can overcome this difficulty by adopting the signal-averaging method developed in rheo-optical studies of dynamic wide-angle X-ray diffraction by Kawai et al.[58] and in dynamic LS studies by Hashimoto et al.[59]

The method[19] to be employed here involves signal accumulation during the relaxation process over repetitive pressure-jump experiments between the two equilibrium states at P_H and at P_L, as shown in Figure 21. The figure involves signal averaging over 20 runs of the pressure jump from P_H to P_L ($j = 1 - N, N = 20$), each run consisting of 50 time slices ($i = 1 - 50$) with a 20-s data-acquisition time per slice and a 5-s interval between the successive slices. The time slicing periods (i) at different relaxation runs (j) were synchronized. The signal-averaged SANS profile $I(q,t)$ at time t is given by

$$I(q, t_i) = \sum_{j=1}^{N} I_j(q, t_i)/N \quad (i = 1 - 50, N = 20) \quad (50)$$

where time t_i is taken at the beginning of ith data acquisition in each relaxation experiment (j). To avoid some artifacts involved by the signal-average process, we confirmed the identity of the equilibrium scattered intensity at 80.0 P_H and 0.1 MPa P_L at 298.1 K and at 100.0 P_H and 0.1 MPa P_L at 309.0 K in each run j of the relaxation experiments. The SANS experiments were carried out with the continuous neutron source at the JRR-3M reactor at JAERI (Japan Atomic Energy Research Institute, Tokai, Japan) with the SANS-U of the ISSP (Institute of Solid State Physics, University of Tokyo). A strong pulse neutron source would be ideal for this kind of relaxation experiment.

Results and discussion

The DPB/PI mixture had an LCST-type phase diagram, and its T_s at 0.1 MPa was 314.2 K. We installed the molded sample of the mixture into the pressure cell, according to a method described in detail elsewhere,[19] which was specially designed for SANS measurements under high pressure (up to 200 MPa) and at high temperatures (up to 523 K). The details of the cell for high pressures and temperatures are reported elsewhere.[60] We measured the pressure dependence of the SANS intensity at 298.1 and 309.0 K to investigate the pressure dependence of the Flory–Huggins segmental interaction parameter χ between DPB and PI. The pressures used here were 0.1, 20.0, 40.0, 60.0, and 100.0 MPa at 309.0 K. For this purpose, the SANS scattered intensity distribution was measured for 30 min at each temperature and at each pressure. The best fit of the SANS profiles with the RPA theory yielded χ as a function of pressure P:[19]

$$\chi = 6.44 \times 10^{-4} - 1.71 \times 10^{-6} \times P \text{ (MPa)} \quad \text{at 298.1 K} \quad (51)$$

and

$$\chi = 7.29 \times 10^{-4} - 8.74 \times 10^{-7} \times P \text{ (MPa)} \quad \text{at 309.0 K} \quad (52)$$

The χ value thus determined decreases with P, and this indicates that the DPB/PI mixture had an upper critical solution pressure (UCSP) phase diagram.

Figure 22 shows χ at the spinodal point (χ_s; solid line) plotted as a function of ϕ_{DPB} for the DPB/PI mixture. The spinodal line was calculated with the following equation:

$$\chi_s = \frac{\nu_0}{2}\left[\frac{1}{\phi_{DPB}\nu_{DPB}N_{w,DPB}} + \frac{1}{\phi_{PI}\nu_{PI}N_{w,PI}}\right] \quad (53)$$

The ordinate axis on the rhs of the figure corresponds to the temperature at 0.1 MPa calculated from the following temperature dependence of χ at 0.1 MPa, which in turn was measured from SANS experiments with the same blend in the single-phase state at 0.1 MPa as a function of temperature:

$$\chi = 2.69 \times 10^{-4} - 0.606/T \quad \text{at 0.1 MPa} \quad (54)$$

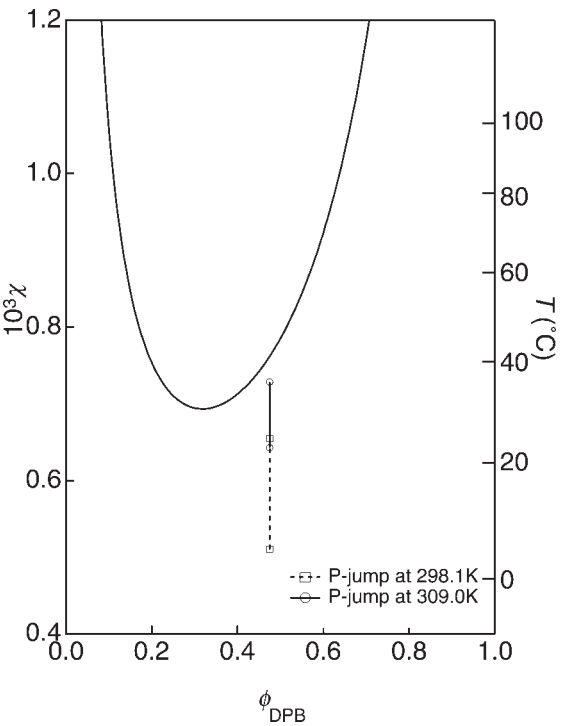

Figure 22. Phase diagram of a DPB/PI blend in the parameter space of χ (left ordinate) or T (°C) at 0.1 MPa (right ordinate) and the volume fraction of DPB in DPB/PI. The solid line indicates the spinodal line of the DPB/PI blend calculated with the Flory–Huggins theory. The broken line with squares and the solid line with circles represent the quench depth in χ due to the pressure jumps at 298.1 and 309.0 K, respectively (from ref. 19).

The figure also includes changes in the thermodynamic state of the blend induced by the pressure jump from 80.0 to 0.1 MPa at 298.1 K and from 100.0 to.1 MPa at 309.0 K, which were estimated from eqs 51 and 52, respectively. The pressure jump from 80.0 to 0.1 MPa at 289.1 K and that from 100.0 to 0.1 MPa at 309.0 K correspond to the sudden increase in the χ value by $\Delta\chi = 1.37 \times 10^{-4}$ and $\Delta\chi = 8.73 \times 10^{-5}$, respectively, or to the sudden temperature increase by $\Delta T = 20.1$ K and $\Delta T = 13.0$ K, respectively, toward the spinodal point from eqs 51, 52, and 54. Thus, the composition fluctuations increase with time after the pressure jump, and accordingly, the SANS intensity increases with time.

For the relaxation process of the composition fluctuations in the single-phase state, as observed with time-resolved SANS, (1) $\delta\phi(\mathbf{r},t)$ is small, so that the linearized time-evolution equation should work well, and (2) the length scale of observation involved in the SANS q range is small,

so that the hydrodynamic interactions may not play an important role. Consequently, the process is well approximated by eq 15. Because $I(q,t)$ is given by

$$I(q, t) \propto \langle|\delta\phi(q, t)|^2\rangle \tag{55}$$

eqs 15 and 55 give the time evolution of $I(q,t)$ in the relaxation process:

$$I(q, t) = I(q, \infty) + [I(q, 0) - I(q, \infty)]\exp[-2R(q)t] \tag{56}$$

where $I(q,0)$ is the scattering intensity profile at $t = 0$ right after the onset of the pressure jump and $I(q,\infty)$ is the equilibrium scattering intensity profile at $t = \infty$ after the pressure jump. $R(q)$ is the relaxation rate of the q Fourier mode of the fluctuations:

$$R(q) = \Lambda_{\text{eff}}(q)q^2(-r_0 + Cq^2) \tag{57}$$

where

$$\Lambda_{\text{eff}}(q) \equiv \Lambda(q)/(1 + \xi_{ve}^2 q^2) \tag{58}$$

The mean-field theory gives

$$-r_0 = \frac{2k_BT}{\nu_0}(\chi_s - \chi),\ C = \frac{2k_BT}{\nu_0}\frac{a^2}{36\phi(1-\phi)} \tag{59}$$

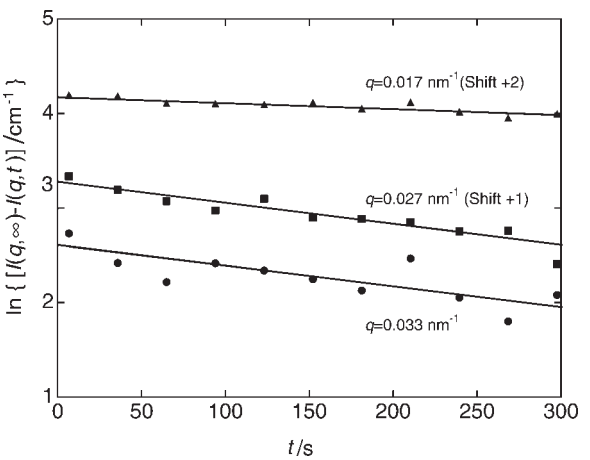

Figure 23. $\ln[I(q,\infty) - I(q,t)]$ plotted as function of time t at 298.1 K and at fixed q values for a DPB/PI blend. The solid lines were obtained by a linear regression of the data (from ref. 19).

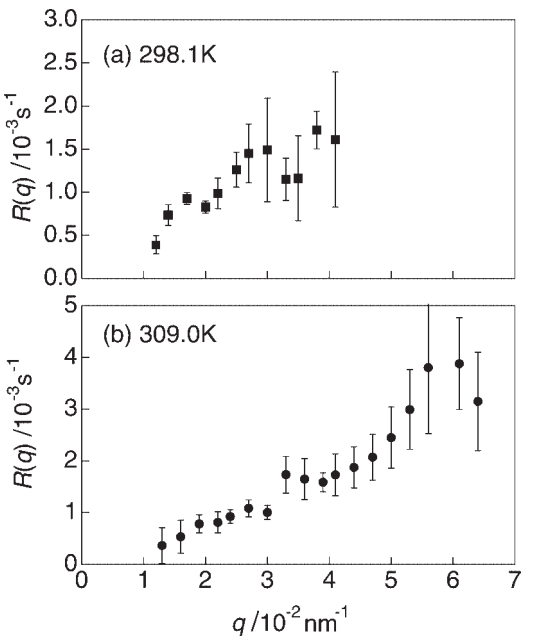

Figure 24. $R(q)$ for the q Fourier mode of the concentration fluctuations plotted as a function of q for a DPB/PI blend at (a) 298.1 and (b) 309.0 K (from ref. 19).

Because $I(q,t)$ increases after the pressure jump, we rearrange eq 56 to obtain

$$\ln[I(q, \infty) - I(q, t)] = \ln[I(q, \infty) - I(q, 0)] - 2R(q)t \tag{60}$$

Therefore, the intensity of $I(q,\infty) - I(q,\infty)$ plotted with a logarithmic scale linearly decreases with t after the onset of the pressure jump, the rate of which gives the relaxation rate $R(q)$.

Figure 23 presents a typical plot of $\ell n[I(q,\infty) - I(q,t)]$ versus t for the time change in the SANS intensity profile for the DPB/PI mixture.[19] The equilibrium intensity $I(q,\infty)$ can be obtained with a high accuracy, and this is a big advantage for this analysis. Although the data are somewhat scattered, a linear reduction has been found, as expected from eq 60, giving rise to a natural trend: the larger q is, the larger $R(q)$ is, as predicted from eqs 57 and 59.

Figure 24 shows the q dependence of $R(q)$ estimated from plots of $\ln[I(q,\infty) - I(q,t)]$ versus t.[19] In both experiments, $R(q)$ increases with q, as expected from the term $q^2(-r_0 + Cq^2)$ in eqs 57 and 59. The values of $R(q)$ at 309.0 K [Fig. 24(b)] are comparable to those at 298.1 K [Fig. 24(a)] in the observed q range, and this seems to indicate

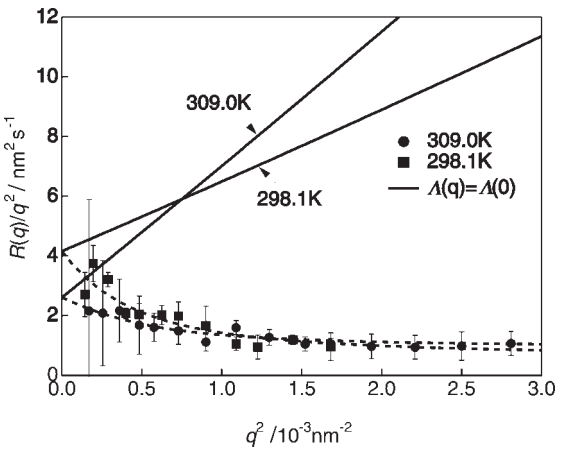

Figure 25. $R(q)/q^2$ plotted against q for a DPB/PI blend at 309.0 and 298.1 K. The solid lines represent $\Lambda(q) = \Lambda(0) = (5.34 \pm 0.74) \times 10^{-22}$ at 298.1 K and $\Lambda(q) = \Lambda(0) = (10.3 \pm 0.6) \times 10^{-21}$ at 309.0 K, and the broken line are visual guides (from ref. 19).

that the critical slowing down cannot be clearly observed. This may be primarily because 309.0 K is not close enough to 314.2 K (T_s) and also because the increase in the Onsager kinetic coefficient term [$\Lambda_{eff}(q)$] with the temperature dominates the reduction in the term $-r_0 + Cq^2$ with the temperature (see eq 57).

Now let us consider the q dependence of $R(q)/q^2$. From eqs 57–59, it follows that

$$\frac{R(q)}{q^2} = \Lambda_{\text{eff}}(q)\frac{2k_BT}{\nu_0}(\chi_s - \chi)(1 + \xi_T^2 q^2) \quad (61)$$

ξ_T for the composition fluctuations is given by

$$\xi_T \equiv \frac{a^2}{36\phi(1-\phi)(\chi_s - \chi)} \quad (62)$$

In the limit of $q \to 0$, we expect a linear increase of $R(q)/q^2$ with q^2, simply because $\Lambda_{eff}(q \to 0)$ in eq 58 becomes constant:

$$\lim_{q\to 0}\Lambda_{\text{eff}}(q) = \lim_{q\to 0}\Lambda(q) \equiv \Lambda(0) = \phi_A(1-\phi_A) \times [D_A N_A(1-\phi_A) + D_B N_B \phi_A]\frac{\nu_0}{k_BT} \quad (63)$$

In reality, as shown in Figure 25, $R(q)/q^2$ nonlinearly decreases with q^2, rather than linearly increasing; that is, the $R(q)/q^2$ values are more suppressed than expected from the linear relationship [as shown by solid lines with $\Lambda_{eff}(q) = \Lambda(0)$], even at q^2 values much smaller than $1/R_g^2$ (2.27×10^{-3} nm^{-2} for DPB and 1.11×10^{-2} nm^{-2} for PI).[19] This means that the Onsager kinetic coefficient must have a strong q dependence for some reason, so that $R(q)$ is strongly suppressed even in the q range of $qR_g < 1$. The larger q is, the larger the suppression degree is.

The q dependence of the Onsager kinetic coefficient [$\Lambda_{eff}(q)$] can be estimated from the measured values of $R(q)/q^2$ and the known static quantities with eqs 61 and 62. The results[19] are plotted in Figure 26, together with theoretical predictions given by Pincus[7] for dynamically symmetric mixtures and by the Doi–Onuiki (DO) theory.[12–14] The experimental value of $\Lambda_{eff}(q)$ is very much suppressed from the constant level of $\Lambda(0)$, as we expected from the results shown in Figure 25.

Pincus-deGennes derived the q dependence of the Onsager kinetic coefficient for dynamically symmetric entangled polymer mixtures in the melt with reptation dynamics:[3,4]

$$\Lambda(q) = \Lambda(0)\frac{1 - \exp(-q^2R_\Lambda^2)}{q^2R_\Lambda^2} \quad (64)$$

where the characteristic length R_Λ in this theory is R_g of the polymers themselves. Although the Pincus theory cannot be applied to our systems,

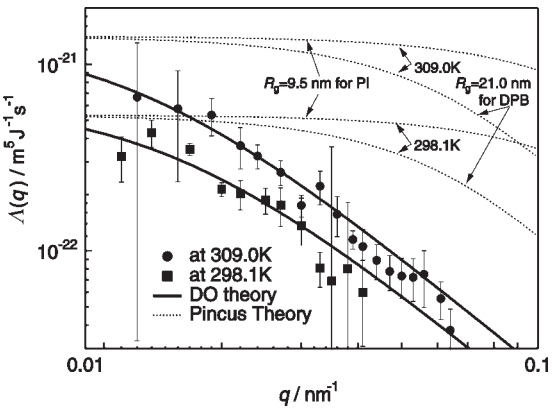

Figure 26. q dependence of $\Lambda(q)$ at 309.0 and 298.1 K for a DPB/PI blend. The solid lines indicate the fitting results from the DO theory (eqs 58 and 63), with the $\Lambda(0)$ and ξ_{ve} values given in the text, whereas the broken lines indicate the prediction of the Pincus theory for the symmetric mixtures, with $\Lambda(0)$ given in the text and R_g values of 9.5 and 21 nm, free from viscoelastic effects (from ref. 19).

we have attempted to elucidate qualitatively the significance of the result of eq 64 for the interpretation of the experimental results. For the experiment at 309.0 K, if we assume $R_\Lambda = R_g = 9.5$ nm for both PI and DPB, we obtain the prediction given by the top dotted line. On the other hand, if we assume $R_\Lambda = R_g = 21.0$ nm for both PI and DPB, we obtain the prediction given by the second dotted line from the top. In this case, $\Lambda(q)$ is given by q^{-2} at $qR_g > 1$, as is clear from eq 64. The same applies to the experiment at 298.1 K. It is clarified that for both cases $\Lambda(q)$ derived for symmetric mixtures undergoing reptation dynamics cannot explain the large suppression of $\Lambda_{eff}(q)$ from $\Lambda(0)$. The large suppression experimentally found must be explained by factors other than the reptation dynamics.

Because it is clarified that $\Lambda(q)$ given by eq 64 is approximately constant over the q range in which the suppression is observed, we assume that $\Lambda(q)$ in eq 64 is a constant given by eq 63 for further analyses of $\Lambda_{eff}(q)$. We fit the experimental results of $\Lambda_{eff}(q)$ with eq 58 under the assumption of $\Lambda(q)$ being equal to $\Lambda(0)$ given by eq 63 and with ξ_{ve} as an adjustable parameter. The best fitting results are displayed by the solid lines in Figure 26. The DO theory can well predict the experimental results for $\Lambda_{eff}(q)$. The estimated $\Lambda(0)$ and ξ_{ve} values are $(6.39 \pm 1.4) \times 10^{-22}$ m^5 J^{-1} s^{-1} and 64.6 ± 12.6 nm, respectively, at 298.1 K and $(14.1 \pm 1.7) \times 10^{-22}$ m^5 J^{-1} s^{-1} and 76.9 ± 7.1 nm, respectively, at 309.0 K. ξ_{ve} is much lager than R_g of DPB and PI, and this shows that the viscoelastic effects play a dominant role in the observed q dependence of the Onsager kinetic coefficient. The effects suppress the transport coefficient even at $qR_g \ll 1$ as ξ_{ve} is large.

In contrast, the Pincus theory predicts the suppression of the kinetic coefficient only at $q \geq 1/R_g$, as he expected. This is natural and reasonable because, when the component polymers are symmetric, α_a goes to zero and hence ξ_{ve} goes to zero; this results in a complete screening of the viscoelastic effects. Thus, the suppression of the kinetic coefficient occurs only through the q dependence of the reptation modes. In other words, the physical origin of the suppression is completely different. In our asymmetric mixtures, the suppression of $\Lambda(q)$ at $1/\xi_{ve} < q < 1/R_g$ reflects the viscoelastic effect, although that at $q \geq 1/R_g$ would be affected by the q dependence of the reptation modes as well. The ξ_{ve} values estimated here are consistent with values independently measured by other methods, as detailed elsewhere.[19]

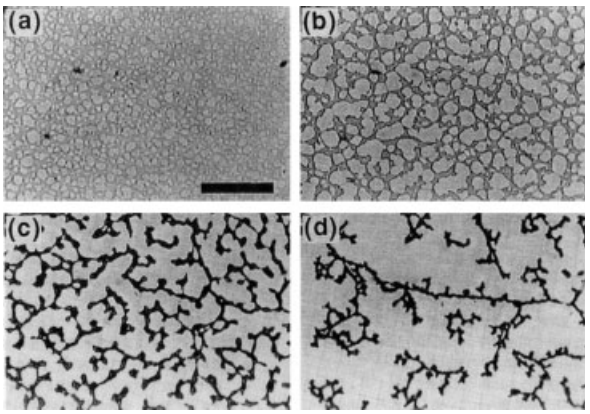

Figure 27. Unique phase-separation structures observed for an aqueous solution of poly(vinyl methyl ether) under transmission light microscopy. Parts a–d were observed 1, 1.4, 3, and 30 s after phase separation at 310.3 K. The scale bar represents 200 μm (from ref. 61).

Further Comments on the Viscoelastic Effects

How do the viscoelastic effects affect pattern formation in the phase-separation process? Figure 27 presents unique phase-separating structures observed under transmission light microscopy for an aqueous solution of poly(vinyl methyl ether).[61] The series of images shows an isothermal time evolution of the structures in the late stage of SD. In this experiment the solution was quenched deeply to a particular temperature (310.3 K, well above T_g) in the spinodal region. The bright phase corresponds to the solvent-rich phase, and the dark phase corresponds to the polymer-rich phase. The two phases form a cocontinuous pattern in which the minority phase of the polymers form continuous network structures in 3D space [Fig. 27(a,b)]. As the networks grow, driven by a thermodynamic force, networks are locally broken and lose their continuity with time [Fig. 27(c,d)], eventually collapsing into droplets rich in polymer. The droplets are coarsened through diffusion and coalescence, although the growth process of droplets in the hydrodynamic regime is not presented in Figure 27.

The cocontinuous structure shown in Figure 27 for the asymmetric system is quite different from that shown in Figure 11 for the symmetric mixtures, which are characterized by a smooth, hyperbolic interface, as more clearly highlighted in

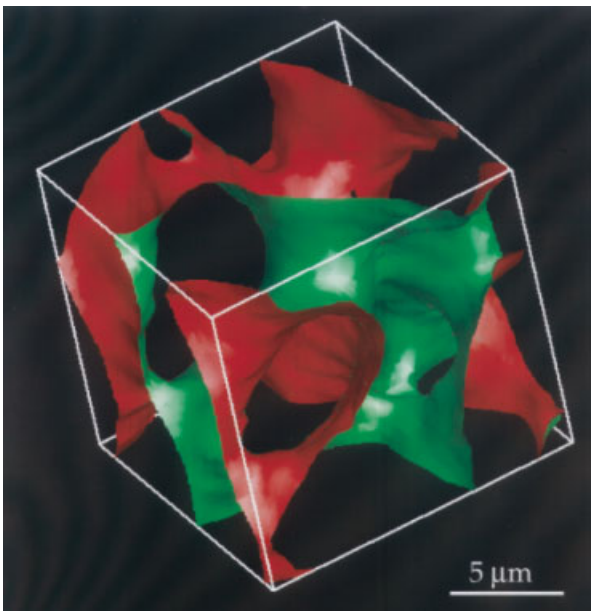

Figure 28. 3D real-space structure of the interface of a PB/SBR mixture developed in the late stage of SD and constructed from LSCM. One side of the interface is colored red, and the other side is green. The mixture approximately satisfies dynamic symmetry, and the interface has a smooth, hyperbolic characteristic with a negative Gaussian curvature (from ref. 50).

Figure 28 for a PB/SBR[50] mixture approximately satisfying dynamic symmetry. The figure represents the interface of the 3D phase-separated structure in the late stage of SD. The 3D image of the interface was constructed from a series of sliced images obtained by LSCM. The image shows the phase-separated structure over approximately one characteristic length Λ_m. One side of the interface is colored red, providing space available for one component in the mixture, and the other side is colored green, providing space available for the other component. The two domains are cocontinuous in 3D space, and the interface is essentially characterized by a smooth, hyperbolic interface with a negative Gaussian curvature.

The network structure in Figure 27(a,b) consists of threads between the network junction points. If the threads consist of a viscous liquid, the interface is expected to be smooth and the threads are expected to have a more uniform diameter than in Figure 27. However, the threads in Figure 27 do not show smooth and uniform characteristics, and this is believed to be a result of the threads consisting of the viscoelastic solutions of entangled polymers. The entangled polymer chains in the threads are pulled apart during the growth process of the threads. The local stress built up by the elastic effects and its stress relaxation due to viscous flow via the disentanglements and/or squeezing of solvents from the threads cause local thinning and thickening of threads, hence developing nonuniformity for the thread diameter and an irregular appearance for the interface. The viscoelastic interactions of the threads appear to extend over a quite long range, involving intrathread and interthread interactions. The viscoelastic length may characterize this interaction range. The pattern formation and growth may involve solvent squeezing from the threads, which are domains rich in polymers, as a result of dynamic asymmetry and take a nonequilibrium pathway, along which the stored elastic energy is dissipated most efficiently.

Cocontinuous phase-separating structures for symmetric mixtures grow with dynamic self-similarity. On the other hand, the dynamically asymmetric system does not seem to strictly obey this rule; a violation of this growth rule seems to be obvious in the later time of the late stage, as shown in Figure 27(c,d), as the system eventually is transformed into a cluster of droplets rich in the polymer in the matrix rich in water.

The patterns shown in Figure 27 are those in a very late stage SD and hence have Λ_m in the range between 20 and 200 μm, almost macroscopic sizes. What kind of phase-separation processes can we imagine in the stage earlier than the stage shown in Figure 27 for dynamically asymmetric systems? The processes have been essentially left unexplored despite physical significances. The processes, dynamics, and patterns in this stage can be best studied with the time-resolved scattering methods. The suppression of the growth rate of q Fourier modes of the fluctuations with q satisfying $q\xi_{ve} > 1$ is anticipated to give a unique time evolution of the scattering profiles $I(q,t)$. Figure 29 shows a typical example for the time evolution of LS profiles for a dynamically asymmetric system in the early stage of SD [Fig. 29(a)] and in the later stages [the intermediate and late stages; Fig. 29(b)].[18] The system investigated here is a 6.0 wt % solution of high-molecular-weight polystyrene (PS; $M_w = 5.48 \times 10^6$, $M_w/M_n = 1.15$) in dioctyl phthalate (DOP). This concentration was 6.7 times higher than the overlap concentrations of polymer coils,[3] so the PS chains were highly entangled. The solution had a cloud temperature (T_{cl}) of 13.8 °C and was quenched below T_{cl} by $\Delta T \equiv T_{cl} - T = 3$ and 1.5 °C from 20 °C, well above T_{cl}.

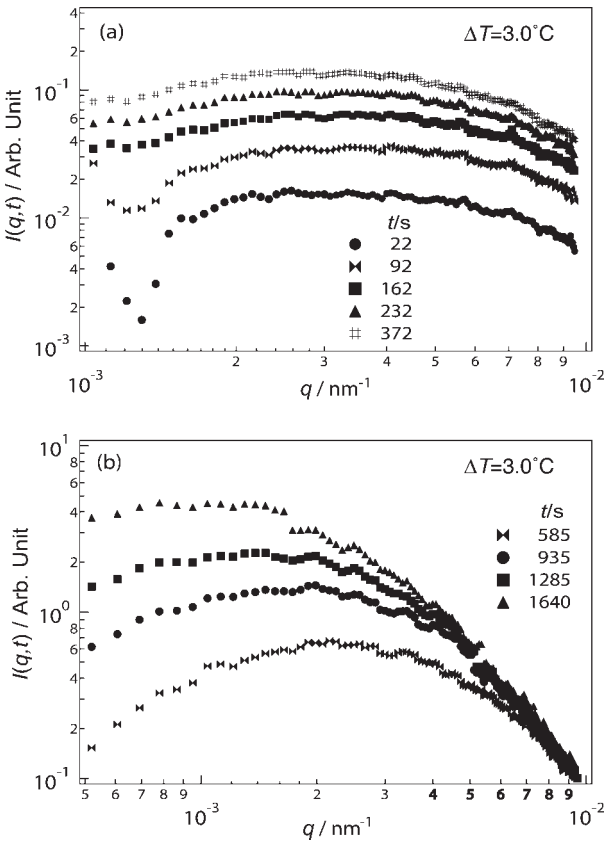

Figure 29. Changes in the LS profiles with time during (a) an early stage and (b) a later stage of the phase-separation process of PS/DOP via SD after the quench from 20.0 to 10.8 °C. ΔT is the quench depth from the cloud-point temperature (13.8 °C; from ref. 18).

As shown in Figure 29(a), in the early stage of SD, the LS profile shows a very broad scattering maximum, so broad that the maximum is less distinct than that for typical symmetric mixtures (see Fig. 14[45] and other cases[62,63]), although the time evolution is well characterized by the CHC theory. This is because ξ_{ve} for this system is 1.04×10^3 nm, as discussed later, and so growth rate $R(q)$ is suppressed for all q's covered in Figure 29 because of the viscoelastic effect, but the degree of the suppression of the rate increases with increasing q. $R(q)$ is small but is less suppressed for the small q modes of $q \cong 10^{-3}$ nm^{-1}, whereas it is high but more suppressed for the large q modes of $q \cong 8 \times 10^{-3}$ nm^{-1}; this gives rise to the observed broadening of the scattering maximum. The time evolution in $I(q,t)$ in the later stage shown in Figure 29(b) is more unique than in the early stage. Because of the aforementioned viscoelastic effect on $R(q)$, the Fourier modes with small q values grow more quickly than those with large q values, and so the scattering maximum becomes less distinct with time. This time evolution in $I(q,t)$ is quite different from that found for dynamically symmetric systems [see Figs. 5 (upper half), 9, and 14], which follow dynamic self-similarity. Apparently, dynamic self-similarity is not fulfilled in dynamically asymmetric systems: the scaled structure factor $F(x)$ is not universal with t. This trend is clearly shown in Figure 27 as well, in which the distribution of the mesh size of the networks becomes broader with time or structure units with larger length scales become more remarkable with time.

The analysis of $I(q,t)$ in the early stage of SD shown in Figure 29(a) with the CHC linearized theory yields $R(q)$ (Fig. 30) and $\Lambda_{eff}(q)$ (Fig. 31).[18] The solid lines in Figure 30 and the solid line and dashed–dotted line in Figure 31 were theoretically predicted with $\xi_{ve} = 1.04 \times 10^3$ nm at 10.8 °C and 9.5×10^2 nm at 12.3 °C, whereas the two broken lines in Figure 30 and the broken horizontal line in Figure 31 indicate the corresponding curves for $\xi_{ve} = 0$. A comparison of the experimental results with those calculated for $\xi_{ve} = 0$ shows that the viscoelastic effect strongly suppresses $\Lambda_{eff}(q)$ and hence $R(q)$ for all the q modes, including those with $qR_g < 1$, $R_g = 63$ nm, covered in this work and that a degree of the suppression increases with q, simply because ξ_{ve} is quite large ($\xi_{ve}/R_g \cong 14$). The viscoelastic effect reduces the wave number $q_m(0)$ of the dominant Fourier modes having a maximum growth rate in the early stage of SD by a factor of about 4, from about 8×10^{-3} nm^{-1} for $\xi_{ve} = 0$ to about 2×10^{-3} nm^{-1} in the real system. The effect also yields a strong downward curvature[18] for the Cahn plot of $R(q)/q^2$ versus q^2 (which is not shown here), in comparison with the case of $\xi_{ve} = 0$, which predicts linear decay.

Figure 32 shows the pattern formation of aqueous dispersions of ionic colloids as observed by LSCM.[64] We carefully matched the density of the colloidal particles with that of the medium by mixing H_2O and D_2O in an appropriate ratio to avoid gravitational effects. The concentration of the colloid was 0.1 vol %, and the salt concentration was $2 - 4 \times 10^{-6}$ M. The colloid had a diameter of 0.12 μm and an effective surface charge of 1400 e. The LSCM images show sliced images with a depth resolution of 0.5 μm at a scan time of 1.0 s. The top two images were obtained right after the homogenization of the dispersion via vigorous shaking of the cell en-

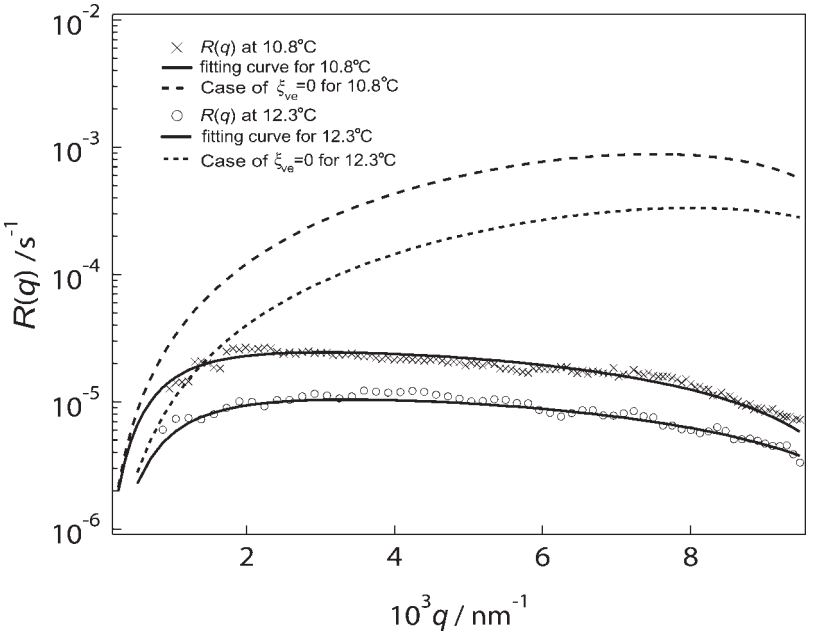

Figure 30. Semilogarithmic plots of $R(q)$ versus q for PS/DOP. The solid lines indicate the values of $R(q)$ calculated with eqs 57–59 and eq 63 with $\xi_{ve} = 1.04 \times 10^3$ nm at 10.8 °C and $\xi_{ve} = 9.5 \times 10^2$ nm at 12.3 °C, whereas the two broken lines indicate the corresponding curves of $R(q)$ for $\xi_{ve} = 0$ (from ref. 18).

closing the sample, whereas the bottom two images were observed 2 months after homogenization. The left and right halves correspond to lower and higher magnifications, respectively. The bright dots are individual particles with a short-range liquidlike order (termed *disordered*

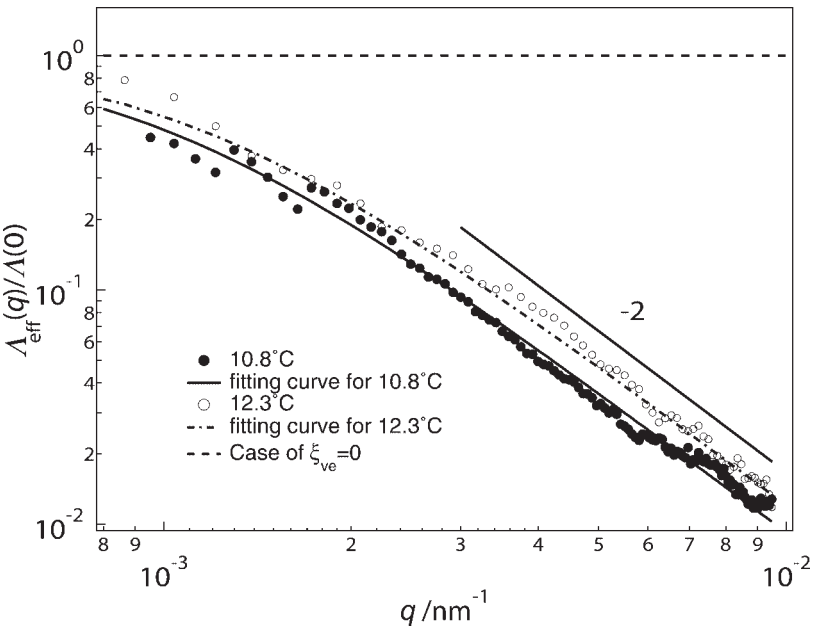

Figure 31. $\Lambda_{eff}(q)/\Lambda(0)$ plotted as a function of q for PS/DOP. The solid line indicates $1/(1 + q^2\xi_{ve}^2)$ with $\xi_{ve} = 1.04 \times 10^3$ nm at 10.8 °C and $\xi_{ve} = 9.5$ ′ 10^2 nm at 12.3 °C, whereas the horizontal broken line represents the case with $\xi_{ve} = 0$ (from ref. 18).

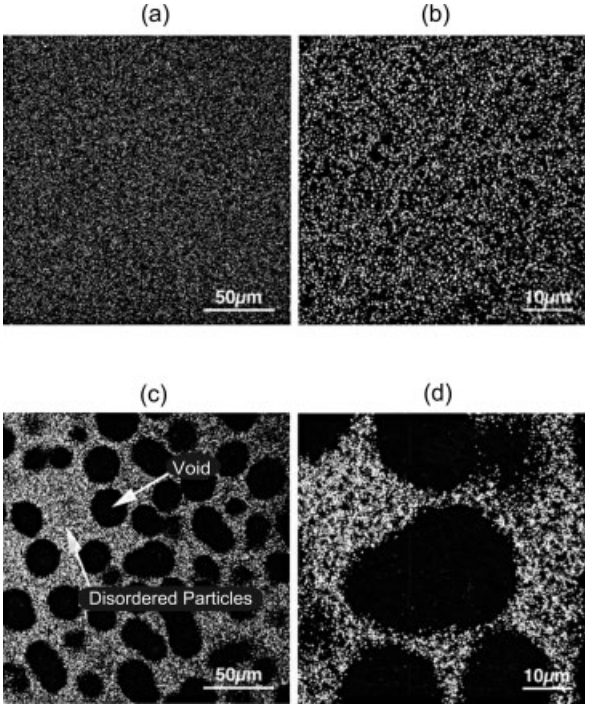

Figure 32. Pattern formation in dilute aqueous dispersions of ionic colloids as observed by LSCM (Data are based on ref. 64).

particles in the figure), and the dark domains are voids free of particles.

The same void structures can be observed everywhere in the dispersion, as shown in Figure 33 by a series of images taken in the same area but with systematic changes in the slicing position along the incident beam from the bottom of the cell. The void size (~30 μm in diameter) is the same everywhere as well. These facts imply that the patterns were formed not by gravitational effects but rather by electrostatic interactions among the particles in the medium, which seems to be effectively attractive. Actually, the voids appearing in the sliced images are not isolated but are rather cocontinuous with the particle-rich region, as is self-evident if we trace the series of images shown in Figure 33. Although the particles are very dilute, they still form domains rich in particles that are continuous in 3D space. The pattern is quite analogous to that formed in the semidilute polymer solution shown in Figure 27(a,b).

The colloidal particles are effectively interconnected by long-range electrostatic interactions with a characteristic time for their spatial rearrangements (τ_{colloid}), as the polymers are interconnected by entanglement couplings with a characteristic time (τ_{rept}). As a result, the concentration fluctuations of the particles or polymers induced in these systems by thermal activation build up local stress. This stress is bared only by the particles or the polymers because of dynamic asymmetry. Thus, a stress imbalance commonly occurs for both systems. The built-up local elastic energy will be dissipated via spatial rearrangements of particles or polymers, and this in turn affects the evolution of the patterns. Thus, the void formation in the colloidal dispersions may be explored from a viewpoint of phase separation involving stress–diffusion coupling and viscoelastic effects and deserves future research.

The suppressed relaxation rate of thermal concentration fluctuations [$R(q)$] makes the dynamically asymmetric systems in a single-phase state very sensitive to shear flow. If the shear rate $\dot{\gamma}$ is smaller than $R(q)$, the q Fourier modes of the concentration fluctuations decay or relax before the shear deforms them. When $\dot{\gamma} < R(q_m)$, is less than $R(q_{\text{m}})$, the maximum relaxation rate, the thermodynamic state of the systems is unaltered. However, when $\dot{\gamma}$ is greater than $R(q_{\text{m}})$, the shear flow affects the concentration fluctuations and hence the state of the systems. Because $R(q_{\text{m}})$ is very much suppressed, even a very small $\dot{\gamma}$ value is sufficient to affect the system state.

Semidilute polymer solutions in a single-phase state become turbid under shear flow with $\dot{\gamma} > \dot{\gamma}_c$,

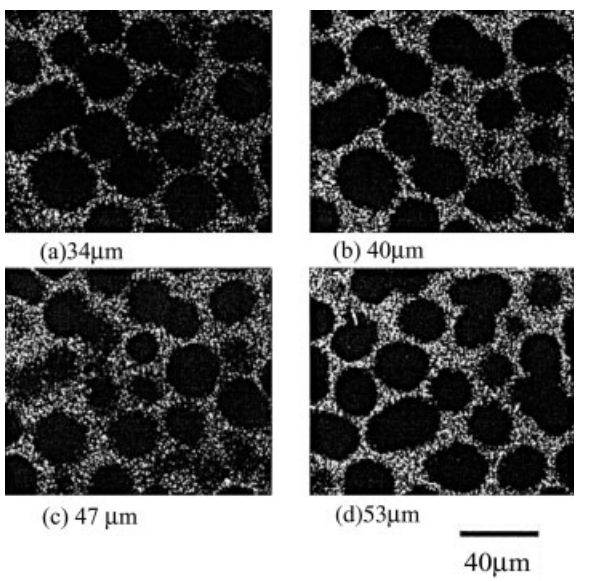

Figure 33. Series of LSCM images taken in the same area with a change in the slicing position from the bottom of the cell along the beam direction for the same dispersions shown in Figure 32.: (a) 34, (b) 40, (c) 47, and (d) 53 μm.

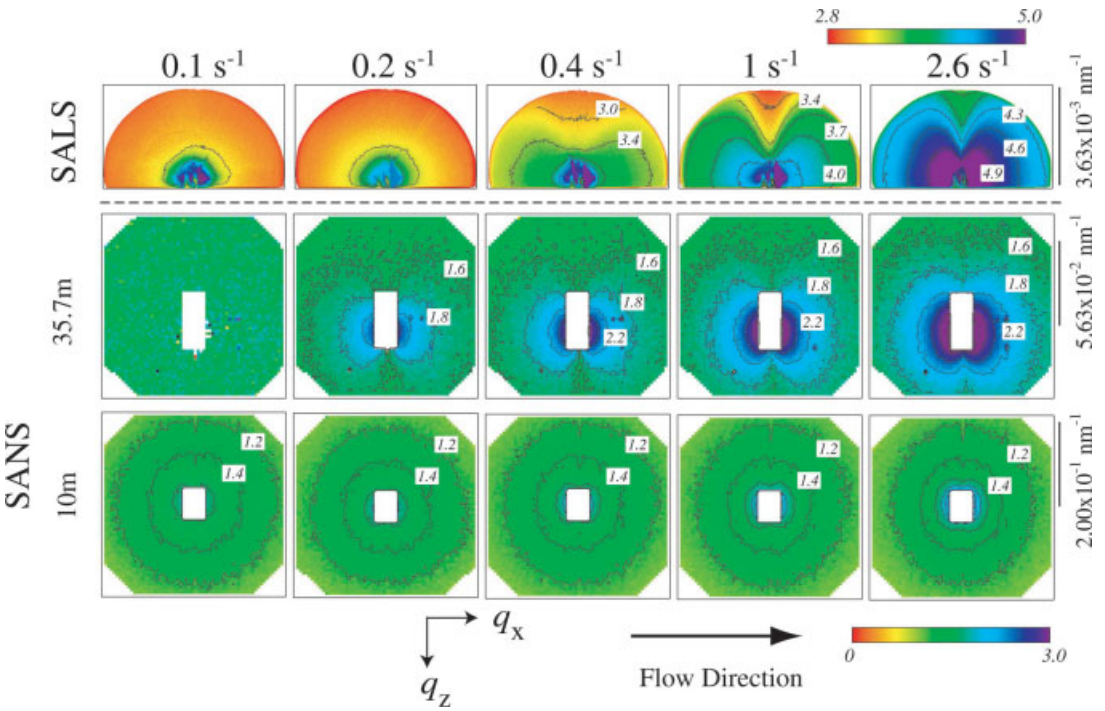

Figure 34. Steady-state SALS and SANS patterns obtained at shear rates of 0.1–2.6 s^{-1} at a given temperature of 22 °C. SANS patterns obtained at different sample-to-detector distances (L = 35.7 or 10 m) are presented. The color bars for the scattering intensity are shown on a logarithmic scale. The values attached to the color bars (absolute units in SANS and arbitrary units in SALS) are the upper and lower limits (from $10^{2.8}$ to $10^{5.0}$ arbitrary units for SALS and from 10^{0} to $10^{3.0}$ cm^{-1} for SANS) of the color histograms. The scale bars attached to the SANS patterns indicate a q scale of 5.63×10^{-2} nm^{-1} for 35.7 m and 2.00×10^{-1} nm^{-1} for 10 m, whereas the scale bar attached to the SALS pattern indicates a q scale of 3.63×10^{-3} nm^{-1}. Based upon ref. 69.

greater than the critical shear rate.[65–67] This intriguing phenomenon of shear-induced turbidity has been explored by *in situ*, real-time observations with SANS,[68,69] LS,[70–72] and optical microscopy.[73,74] Above $\dot{\gamma}_c$, we find shear-rate-dependent dissipative structures (ordered patterns developed in open, nonequilibrium systems) and strong butterfly-type scattering patterns, although below $\dot{\gamma}_c$ the solutions are homogeneous, and no strong scattering can be observed. Figure 34 presents butterfly-type SANS and small-angle light scattering (SALS) patterns[69] observed for the same semidilute PS/DOP solutions discussed previously in conjunction with Figures 29–31. The patterns are observed in the q_z–q_x plane, q_x being **q** along the flow direction and q_z being **q** along the neutral (or vorticity) direction. The velocity gradient exists along the q_y direction. In the quiescent state of $\dot{\gamma} = 0$ s^{-1}, both the SALS and SANS patterns are isotropic, and their intensities are weak (the patterns are not shown in the figure). At $\dot{\gamma} = 0.1$ s^{-1}, there is no change in the shape or intensity, and the flow does not affect the SALS and SANS patterns or, therefore, the concentration fluctuations.

At $\dot{\gamma} = 0.2$ s^{-1}, only the SANS pattern observed at the sample-to-detector distance of L = 35.7 m ($6.76 \times 10^{-3} \leq q \leq 6.00 \times 10^{-2}$ nm^{-1}) shows an anisotropic pattern with a strong intensity along the q_x direction, which is called a butterfly pattern,[70] and without any change in the q_z direction, which is called a dark streak in the butterfly pattern.[70] This indicates that large amplitude concentration fluctuations develop only along the flow direction in the q range covered. In larger ($2.51 \times 10^{-2} \leq q \leq 8.0 \times 10^{-1}$ nm^{-1}) and smaller q regions ($6.27 \times 10^{-4} \leq q \leq 3.63 \times 10^{-3}$ nm^{-1}) covered by SANS with L = 10 m and by SALS, respectively, the shapes and intensities are almost the same as those in quiescent solution, and

this shows that the structures are not much affected by the shear flow in the two corresponding q ranges.

At $\dot{\gamma} = 0.4\ s^{-1}$, the SALS pattern also begins to exhibit the butterfly pattern, revealing that the concentration fluctuations expand to larger length scales. At higher $\dot{\gamma}$ values of 1 and 2.6 s^{-1}, both the SALS pattern and the SANS pattern with $L = 35.7$ m evolve into butterfly patterns in such a way that the scattering intensity along q_x increases and the butterfly wings expand; this results in a narrowing of the dark streak along the q_z direction. On the contrary, the SANS patterns obtained at L values of 10 and 2.5 m (which are not shown in the figure) remain equal to those in the quiescent state, showing that the Fourier modes of the concentration fluctuations in this q region ($2.51 \times 10^{-2} \leq q \leq 7.75 \times 10^{-1}\ nm^{-1}$) are not enhanced at these values of $\dot{\gamma}$.

The butterfly scattering arises from the shear-induced concentration fluctuations that are built up in the systems against the osmotic pressure. Under the shear flow with $\dot{\gamma} > \dot{\gamma}_c$, elastic energy stored by the deformed, swollen, entangled network chains cannot be relaxed via disentanglements because $\dot{\gamma}$ is larger than the disentanglement rate. Thus, the relaxation involves the squeezing of solvents from the swollen entangled networks of polymer chains. Regions rich in polymers are deformed more and hence squeeze solvents more than the regions poor in polymer. Thus, local concentration fluctuations are built up to result in the formation of shear-induced dissipative structures, as observed by the butterfly patterns. The shear-induced structures driven by the viscoelastic effects have been studied under continuous shear flow,[70–75] under oscillatory shear flow,[74,76–78] and as a function of the solvent quality,[79] molecular weight,[70] concentration,[70,80] and so forth. Theories of shear-induced fluctuations were pioneered by Helfand and Fredickson[81] and elaborated by Onuki.[12]

Summary

We have presented time-resolved SANS and LS studies of the dynamics of the composition (or concentration) fluctuations and pattern formation for dynamically asymmetric systems in which the components in the systems have different self-diffusion coefficients. The systems are polymer mixtures, polymer solutions, and aqueous dispersions of ionic colloidal particles. We have discussed the stress–diffusion coupling and viscoelastic relaxations, which are irrelevant to dynamically symmetric systems but play important roles in the dynamics and pattern formation of these systems.

The relaxation or growth rate of the fluctuations [$R(q)$] is suppressed for the Fourier modes with q satisfying $q\xi_{ve} > 1$, where ξ_{ve} is a screening length for the viscoelastic effect called the viscoelastic length: ξ_{ve} can be much larger than R_g's of the component polymer(s). The pattern formation in the two-phase region initially involves the formation of a percolated networklike structure rich in dynamically slow-component units in a matrix rich in fast-component units, as a result of squeezing fast-component units from regions rich in slow-component units. The networklike structures have a rough interface and a large distribution in the mesh size (or network periodicity) as a result of the viscoelastic effects on the growth process. Their growth process does not obey dynamic self-similarity, as found for dynamically symmetric systems. Accordingly, the time evolution of the scattering functions is very different in these two systems. However, we expect that the two systems behave similarly in the long time limit for which $t \gg \tau_{ve} = \xi_{ve}^2/D$ (D is the mutual diffusion coefficient) is true and hydrodynamic interactions dominate the dynamics.

We have briefly pointed out that dynamically asymmetric systems are unique also in their shear-induced structure formation, which causes shear-induced butterfly type scattering patterns, again because of the viscoelastic effects. Finally, we stress that polymers provide good model systems for dynamically asymmetric systems as well because we can easily tune the asymmetry parameter with respect to the molecular weights of polymers and the frictional characteristics of monomer units and because their spatiotemporal scales are quite appropriate for experimental investigations.

The author gratefully acknowledges Charles C. Han, Hiroshi Jinnai, Tsuyoshi Koga, Mikihito Takenaka, and Hirokazu Hasegawa for their contributions to this work. The small-angle neutron scattering (SANS) experiments discussed in this work were performed with 8- and 30-m SANS instruments at the NIST Research Reactor (Gaithersburg, MD), with the SANS-U at JAERI (Tokai, Japan), and with the D11 instrument at the Institute Laue-Langavin ILL (Grenoble, France). This work was partially supported by a Grant-in-Aid for Scientific Research

[12305060(A)]. This article is based on a plenary lecture presented at the 2001 International Conference on Neutron Scattering at Munich Technical University (Munich, Germany).

REFERENCES AND NOTES

1. Gunton, J. D.; San Miguel, M.; Sahni, S. In Phase Transition and Critical Phenomena; Domb, C.; Lebowitz, L., Eds.; Academic: New York, 1983; p 269.
2. Flory, P. J. Principles of Polymer Chemistry; Cornell University Press: Ithaca, New York, 1967.
3. de Gennes, P. G. Scaling Concept in Polymer Physics; Cornell University Press: Ithaca, NY, 1979.
4. Doi, M.; Edwards, S. F. Theory of Polymer Dynamics; Clarendon: London, 1986.
5. Hashimoto, T. In Materials Science and Technology; Cahn, R. W.; Haasen, P.; Kramer, E. J., Eds.; Thomas, E. L., Vol. Ed.; VCH: Weinheim, Germany; 1993; Vol. 12, Chapter 6, p 251.
6. de Gennes, P. G. J Chem Phys 1980, 72, 4756.
7. Pincus, P. J Chem Phys 1981, 75, 1996.
8. Binder, K. J Chem Phys 1983, 79, 6387.
9. Akcasu, A. Z. Macromolecules 1989, 22, 3682.
10. Hashimoto, T.; Koga, K.; Jinnai, H.; Nishikawa, Y. Nuovo Cimento 1998, 20, 1947.
11. Hashimoto, T.; Jinnai, H.; Nishikawa, Y.; Koga, T. Macromol Symp 2002, 190, 9.
12. Onuki, A. Phase Transition Dynamics; Cambridge University Press: Cambridge, England, 2002.
13. Doi, M.; Onuki, A. J Phys II 1992, 2, 1631.
14. Onuki, A. J Non-Cryst Solids 1994, 172, 1151.
15. Tanaka, H. Phys Rev Lett 1993, 71, 3158.
16. Tanaka, H. J Chem Phys 1994, 100, 5253.
17. Tanaka, H. Phys Rev Lett 1996, 76, 787.
18. Toyoda, N.; Takenaka, M.; Saito, S.; Hashimoto, T. Polymer 2001, 42, 9193.
19. Takenaka, M.; Takeno, H.; Haseawa, H.; Saito, S.; Hashimoto, T.; Nagao, M. Phys Rev E 2002, 65, 021806-1.
20. Cahn, J. W. J Chem Phys 1965, 42, 93.
21. Cook, H. E. Acta Metall 1970, 18, 297.
22. Cahn, J. W.; Hilliard, J. E. J Chem Phys 1958, 29, 258.
23. Landau, L. D.; Lifshitz, E. M. Statistical Physics; Pergamon: New York, 1964.
24. Kawasaki, K.; Ohta, T. Prog Theor Phys 1978, 59, 362.
25. Debye, P. J Chem Phys 1959, 31, 650.
26. Hashimoto, T.; Jinnai, H.; Hasegawa, H.; Han, C. C. JAERI-M93-228 Proceedings of the 5th International Symposium on Advanced Nuclear Energy Research, Neutrons as Microscopic Probes, Shirai, E., Ed., Japan Atomic Energy Research Institute, Ibarkiken, Japan, March 1993.
27. Hashimoto, T.; Jinnai, H.; Hasegawa, H.; Han, C. C. Physica A 1994, 204, 261.
28. Higgins, J. S.; Benoit, H. C. Polymers and Neutron Scattering; Clarendon: Oxford, 1994.
29. Jinnai, H.; Hasegawa, H.; Hashimoto, T.; Han, C. C. Macromolecules 1991, 24, 282.
30. Binder, K.; Stauffer, D. Phys Rev Lett 1974, 33, 1006.
31. Binder, K. Phys Rev B 1977, 15, 4425.
32. Chou, Y. C.; Goldburg, W. I. Phys Rev A 1981, 23, 858.
33. Knobler, C. M.; Wong, N.-C. J Phys Chem 1981, 85, 1972,
34. Wong, N.-C.; Knobler, C. M. Phys Rev A 1981, 24, 3205.
35. Jinnai, H.; Nishikawa, Y.; Morimoto, H.; Koga, T.; Hashimoto, T. Langmuir 2000, 16, 4380.
36. Hyde, S.; Anderson, K.; Larsson, K.; Blum, Z.; Landh, T.; Lidin, S.; Ninham, B. W. The Language of Shape; Elsevier: Amsterdam, 1997.
37. Koga, T.; Jinnai, H.; Hashimoto, T. Physica A 1999, 236, 369.
38. Chou, Y. C.; Goldburg, W. I. Phys Rev A 1979, 20, 2105.
39. Langer, L. S.; Bar-on, M.; Miller, H. D. Phys Rev A 1975, 11, 1417.
40. Hashimoto, T. Phase Transitions 1988, 12, 47.
41. Takenaka, M.; Hashimoto, T. J Chem Phys 1992, 96, 6177.
42. Koga, T.; Kawasaki, K. Phys A 1993, 196, 389.
43. Onuki, A. J Chem Phys 1986, 85, 1122.
44. Hashimoto, T.; Itakura, M.; Shimidzu, N. J Chem Phys 1986, 85, 6773.
45. Motowoka, M.; Jinnai, H.; Hashimoto, T. J Chem Phys 1993, 99, 2095.
46. Kirste, B.; Porod, G. Kolloid Z Z Polym 1962, 184, 1.
47. Tomita, H. Prog Theor Phys 1984, 72, 656.
48. (a) Porod, G. Kolloid Z 1951, 124, 83; (b) Porod, G. Kolloid Z 1952, 125, 51; (c) Porod, G. Kolloid Z 1952, 125, 108.
49. Takenaka, M.; Hashimoto, T. Physica A 2000, 276, 22.
50. Hashimoto, T.; Jinnai, H.; Nishikawa, Y.; Koga, T.; Takenaka, M. Prog Colloid Polym Sci 1997, 106, 118.
51. Nishikawa, Y.; Koga, T.; Hashimoto, T.; Jinnai, H. Langmuir 2001, 17, 3254.
52. (a) Hashimoto, T.; Todo, A.; Itoi, H.; Kawai, H. Macromolecules 1977, 10, 377; (b) Hashimoto, T.; Fujimura, M.; Kawai, H. Macromolecules 1980, 13, 1660.
53. Rathje, J.; Ruland, W. Colloid Polym Sci 1976, 254, 358.
54. Takenaka, M.; Hashimoto, T. J Chem Phys 1992, 96, 6177.
55. Joanny, J. F.; Leibler, L. J Phys (Paris) 1978, 39, 951.
56. Abraham, F. F.; Nelson, D. R. J Phys (France) 1990, 51, 2653.

57. Wen, X.; Garland, C. W.; Hwa, T.; Kardar, M.; Kokufuta, T.; Li, Y.; Tanaka, T. Nature 1992, 355, 426.
58. (a) Kawai, H.; Itoh, T.; Keedy, D. A.; Stein, R. S. Polym Lett 1964, 2, 1075; (b) Kawaguchi, T.; Itoh, T.; Kawai, H.; Keedy, D. A.; Stein, R. S. Macromolecules 1968, 1, 126; (c) Kawai, H.; Nomura, S.; Hashimoto, T.; Suehiro, S.; Fujita, K. In High Modulus Polymers; Zachariades, A. E.; Porter, R. S., Eds.; Marcel Dekker: New York, 1988; Chapter 12, p 363.
59. (a) Hashimoto, T.; Prud'homme, R.; Keedy, D. A.; Setin, R. S. J Polym Sci Polym Phys Ed 1973, 11, 693; (b) Hashimoto, T.; Prud'homme, R.; Stein, R. S. J Polym Sci Polym Phys Ed 1973, 11, 709.
60. Takeno, H.; Nagao, M.; Nakayama, Y.; Hasegawa, H.; Hashimoto, T.; Seto, H.; Imai, M. Polym J 1997, 29, 931.
61. Tanaka, H. Macromolecules 1992, 25, 6377.
62. Hashimoto, T.; Kumaki, J.; Kawai, H. Macromolecules 1983, 16, 641.
63. Izumitani, T.; Hashimoto, T. J Chem Phys 1985, 83, 3694.
64. Yoshida, H.; Ise, N.; Hashimoto, T. J Chem Phys 1995, 103, 10146.
65. Ver Strate, G.; Phillipoff, W. J Polym Sci Polym Lett Ed 1974, 12, 267.
66. Schmidt, R.; Wolf, B. A. Colloid Polym Sci 1979, 257, 1187.
67. Rangel-Nafaile, C.; Metzner, A. B.; Wissbrun, K. F. Macromolecules 1984, 17, 1187.
68. Morfin, I.; Lindner, P.; Boue, F. Macromolecules 1999, 32, 7208.
69. Saito, S.; Hashimoto, T.; Morfin, I.; Lindner, P.; Bouè, F. Macromolecules 2002, 35, 445.
70. Hashimoto, T.; Fujioka, K. J Phys Soc Jpn 1991, 60, 356.
71. Wu, X.-L.; Pine, D. J.; Dixon, P. K. Phys Rev Lett 1991, 66, 2408.
72. Hashimoto, T.; Kume, T. J Phys Soc Jpn 1992, 61, 1839.
73. Moses, E.; Kume, T.; Hashimoto, T. Phys Rev Lett 1994, 72, 2037.
74. Matsuzaka, K.; Hashimoto, T. Rev Sci Instrum 1999, 70, 2387.
75. Kume, T.; Hashimoto, T.; Takahashi, T.; Fuller, G. G. Macromolecules 1997, 30, 7232.
76. Saito, S.; Matsuzaka, K.; Hashimoto, T. Macromolecules 1999, 32, 4879.
77. Saito, S.; Koizumi, S.; Matsuzaka, K.; Suehiro, S.; Hashimoto, T. Macromolecules 2000, 33, 2153.
78. Saito, S.; Hashimoto, T.; Morfin, I.; Lindner, P.; Bouè, F.; Pine, D. J. Macromolecules 2003, 36, 3745.
79. Endoh, M.; Saio, S.; Hashimoto, T. Macromolecules 2002, 35, 7692.
80. Saito, S.; Hashimoto, T. J Chem Phys 2001, 114, 10531.
81. Helfand, E.; Fredrickson, G. H. Phys Rev Lett 1989, 62, 2468.